Impact of ice multiplication on the cloud electrification of a cold-season thunderstorm: a numerical case study

Jing Yang[1,2,#], Shiye Huang[1,#], Tianqi Yang[3], Qilin Zhang[1], ~~Xiaoqin Jing[1],~~ Yuting Deng[1], Yubao Liu[1]

[1]Collaborative Innovation Center on Forecast and Evaluation of Meteorological Disasters (CIC-FEMD)/China Meteorological Administration Aerosol-Cloud and Precipitation Key Laboratory/Precision Regional Earth Modeling and Information Center (PRMIC), Nanjing University of Information Science & Technology, Nanjing, 210044, China.
[2]CMA Cloud-Precipitation Physics and Weather Modification Key Laboratory (CPML), Beijing, 100081, China.
[3]Nanjing Meteorological Bureau, Nanjing, 210019, China
[#]These authors contributed equally to the work

Correspondence to: Yubao Liu (ybliu@nuist.edu.cn)

Abstract. Ice microphysics controls cloud electrification in thunderstorms, and the various secondary ice production (SIP) processes are vital in generating high ice concentrations. However, the role of SIP in cold-season thunderstorms is not well understood. In this study, the impacts of SIP on the electrification in a thunderstorm that occurred in late November are investigated using model simulations. The parameterizations of four SIP processes are implemented in the model, including the rime-splintering, ice-ice collisional breakup, shattering of freezing drops, and sublimational breakup of ice. In addition, a noninductive and an inductive charging parametrization, as well as a bulk discharging model are coupled with the spectral bin microphysics scheme. The macroscopic characteristics and the temporal evolution of this thunderstorm are well modeled. The radar reflectivity and flash rate obtained by adding four SIP processes is more consistent with the observation than that without SIP. ~~The results show the simulated storm intensity and temporal variation of flash rate are improved after SIP parametrizations are implemented in the model.~~ Among the four SIP processes, the rime-splintering ~~and shattering of freezing drops have~~ has the ~~stronger~~ strongest impacts on the storm ~~than the ice-ice collisional breakup and sublimational breakup~~. The graupel and snow ~~concentration~~ concentrations are enhanced while their sizes are suppressed due to the SIP. The changes in the ice microphysics result in substantial changes in the charge structure. The total charge density changes from an inverted tripole structure to a dipole structure (tripole structure at some locations) after four SIP processes are considered in the model, mainly due to the enhanced collision between graupel and ice. These changes lead to an enhancement of the vertical electric field, especially in the mature stage, which explains the improved modeling of flash rate. The results highlight that cold-season cloud electrification is very sensitive to the SIP processes.

1 Introduction

Cold-season thunderstorms may have different characteristics of charge structure and lightning activity from warm-season thunderstorms due to the different thermodynamic conditions (Michimoto, 1991; Takahashi et al., 1999; Caicedo et al., 2018). Caicedo et al. (2018) investigated the differences between cold-season and warm-season thunderstorms in north-central Florida

using the Lightning Mapping Array (LMA) and radar data. They showed an apparent discrepancy is that all the observed charge areas of summer storms were located up to 1 km higher than in winter/spring storms, as well as the 0 °C, -10 °C, and -20 °C isotherms. The average LMA initiation power in winter/spring storms was about an order larger than in summer storms.
35 This result is supported by the electric field measurements of the initial breakdown process by Brook (1992), who assured that cloud-to-ground discharges and intracloud discharges were probably more energetic in winter than in summer. Wang et al. (2021) reported that in contrast to lightning in summer, which mostly delivered negative charges to the ground, 30% of cloud-to-ground lightning in Honshu Island winter thunderstorms delivered positive charges to the ground. They attributed this phenomenon to inverted charge structures. The apparent differences between the cold-season and warm-season thunderstorms
40 indicate different characteristics of ice microphysics that control ~~the~~ cloud electrification.

Extensive studies have been made to understand the role of ice microphysics on cloud electrification in summertime thunderstorms (e.g., Mansell et al., 2010; Fierro et al., 2013; Guo et al., 2005; Qie et al., 2015; 2019; Zhang et al., 2016; Lyu et al., 2023), while fewer have been performed focusing on cold-season thunderclouds. Michimoto (1991) investigated the
45 behavior of both 30 dBZ and 20 dBZ radar echoes in early winter thunderstorms and found that lightning occurred as 30 dBZ radar echo reached -20 °C, from which it could be inferred that lightning was related to the interaction of graupel and ice crystals. Zheng et al. (2018) analyzed the charge distribution of cells in three winter thunderstorms in Hokuriku region of Japan based on LMA and radar data. They suggested ~~the~~ that riming electrification between graupel and ice crystals or their aggregations ~~are~~ is the dominant mechanism for the electrification in most cells, and the charging process between snow
50 aggregates is responsible for ~~some~~ inverted charge ~~structure~~ structures that occurred above 0 °C isotherm. Using a variety of observational data from Video Sounder, Video Sounder-HYVIS, radar, and the Lightning Location System Network, Takahashi et al. (2019) revealed that the frequent lightning activity produced by shallow winter thunderclouds in Hokuriku is probably due to the high number concentration of ice crystals.

55 One of the key mechanisms of ice generation in deep convective ~~cloud~~ clouds is ice multiplication, i.e., secondary ice production (SIP), which means the ice fragments produced during the interactions between different hydrometeors or freezing of supercooled drops. SIP is the main explanation ~~that~~for why the observed ice concentration is orders of magnitude higher than the ice nucleating particles (INP, Hallett and Mossop, 1974; Heymsfield and Willis, 2014; Yang et al., 2016; Korolev and Leisner, 2020). Some studies have tried to investigate the impact of SIP on cloud electrification in summer (e.g., Fierro et al.,
60 2013; Latham et al. 2004; Mansell et al., 2010; Phillips et al., 2020; Phillips and Patade, 2022), mostly based on numerical simulation since a limitation of observation is it can hardly separate different ice generation processes. For example, Latham et al. (2004) investigated the role of the rime-splintering process in lightning activity using model simulation, they suggested that the relationship between flash rate and precipitation intensity is linear if not considering SIP, while this relationship changed to non-linear with the SIP included. However, ~~the~~ rime-splintering is not the only SIP process that can influence the
65 charge structure of thunderstorms. Secondary ice can be produced through various processes, such as the shattering of freezing

drops and, ice-ice collisional breakup, and sublimational breakup of ice (Lauber et al., 2018; Phillips et al. 2018; Korolev and Leisner, 2020; Deshmukh et al., 2022). Recently, Phillips and Patade (2022) showed the ice-ice collisional breakup may significantly alter the charge structure of summertime thunderstorms based on model simulation using a high-resolution cloud model.

Till now, to our best knowledge, no study has investigated the role of different SIP processes in cloud electrification under cold-season condition conditions using numerical simulations. But However, there are a few modelling modeling studies that highlighted the importance of ice generation in wintertime cloud electrification. For example, Takahashi (1983) studied electrical development in winter thunderclouds using an axisymmetric cloud model. The results showed no strong electrification was observed prior to before the appearance of the solids, which implies the importance of the riming-charging for the electrification. Thus, the generation of graupel perhaps plays a vital role in the wintertime cloud electrification, while SIP controls the fast graupel generation in convective clouds (Yang et al., 2016; Takahashi et al., 2019). Using the Regional Atmospheric Modelling System (RAMS) mesoscale forecast model, Altaratz et al. (2005) analyzed the charge separation in winter convections using different parameterizations of noninductive charging mechanism, and they showed the charge structure is very sensitive to the choice of ice microphysics scheme.

In this study, we performed a real-case simulation using Weather Research and Forecast (WRF) model coupled with a fast spectral bin microphysics (SBM) (Khain et al., 2004) and a bulk lightning model (Fierro et al., 2013) to investigate the impacts of SIP on cold-season thunderstorm. Parameterizations of four different SIP processes, an inductive and a noninductive charging parameterization (Saunders and Peck, 1998; Mansell et al., 2005; Mansell et al., 2010) are implemented in the fast-SBM scheme. The SIP processes considered here include rime-splintering, ice-ice collisional breakup, shattering of freezing drops, and sublimational breakup of ice. The rest of the paper is organized as follows: Section 2 describes the model and design of numerical experiments. Section 3 shows the results, including the model validation and the impacts of different SIP processes on cloud microphysics and charge structure. Discussion and conclusions are presented in Section 4. The parameterizations used in this study are detailed in Appendix A and B.

2 Model description and design of numerical experiments

2.1 Case description

On Nov. 27th-28th, 2022, a severe thunderstorm occurred in Southeast China. The storm began at about 15:00 UTC on Nov. 27th, and lasted for more than 18 hours. Figure 1 shows the synoptic conditions at 18:00, Nov. 27th and 00:00, Nov. 28th plotted using NCEP reanalysis data. At 500 hPa, the relative humidity was low in southeast China at 18:00, Nov. 27th (Fig. 1a). Westerly wind prevailed and the temperature ranged from -6 °C to -12 °C. A weak short wave was present between 108 °E and 112 °E, and was moving towards the east. At 850 hPa (Fig. 1b), the southwesterly wind brought warm moist air to southeast

China, and the low-level relative humidity was very high, resulting in a nearly saturated condition. Baroclinicity was present as seen from the wind blowing across the isotherms. The moist low-level and dry high-level conditions are favorable for convection formation. At 00:00, Nov. 28th, two areas with relatively high relative humidity were observed at 500 hPa, especially near Fuyang, where the air was saturated. This is because two convective cells already formed at this time. The low-level southwesterly wind kept providing warm moist air during the development of the convection.
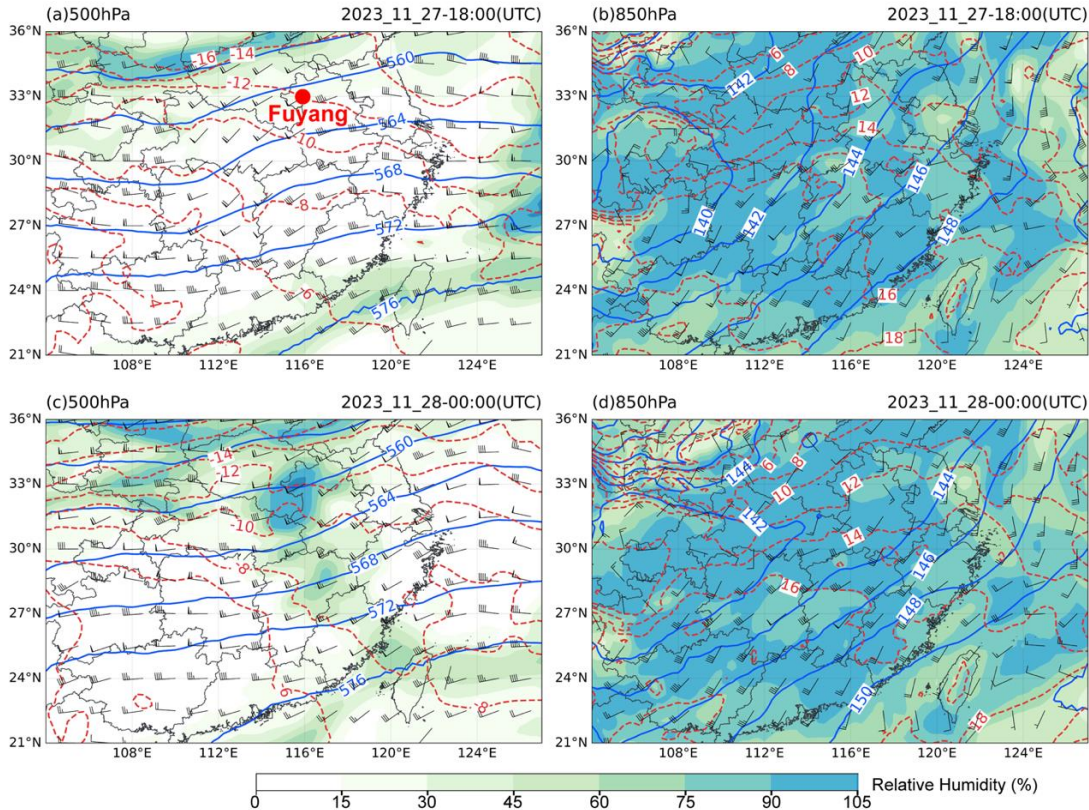
Figure 1: Synoptic conditions of the thunderstorm occurred ~~on Nov. 28th, 2022~~at (a and b) 18:00, Nov. 27th ~~(a and b)~~ and (c and d) 00:00, Nov. 28th ~~(c and d)~~. (a and ~~b~~c) 500 mb geopotential height, isotherms, and wind barbs ~~at 04:00 UTC and 10:00 UTC, respectively~~. (~~c~~ b and d) Same as (a) and (~~b~~c) but for 850 mb. The red dot in (a) indicates the location of the sounding measurement that is shown in Fig. 2.

The synoptic condition is also evident in the sounding measurement. As seen in Figure 2, at 12:00 on Nov. 27th, there was a deep moist layer from the surface up to 700 hPa, and the specific humidity decreased substantially above 700 hPa. The low-level wind was southwesterly and the upper-level wind was westerly. Due to the southwesterly warm air, the temperature near surfaces was approximately 18 °C, which is higher than the typical temperature in November in this region, but is about 10 °C lower than that in summer. Potential instability was present in such a thermodynamic environment, providing favorable conditions for deep convection to occur. At 00:00 on Nov. 28th, the air was nearly saturated below 500 hPa, as the convective

clouds had formed. There was an inversion layer near ~~the~~ surface, probably due to the cold pool induced by the convective precipitation.

The radar composite reflectivity at different times in southeast China is shown in Figure ~~3~~4g-i. At 02:00, Nov. 28th, two deep convective clouds were observed, extending from southwest to northeast and generating lightning flashes (Fig. 2a). The reflectivity in the convective core was approximately 50 dBZ. The entire system moved towards the east, and the east convective cloud moved to the sea after 06:00 (Fig. ~~2c~~4i). The intensity of the storm remained similar between 02:00 and 06:00, while the scale of these two convections slightly increased during the eastward propagation. The storm left the continent and continued on the sea after 08:00, Nov. 28th (not shown).
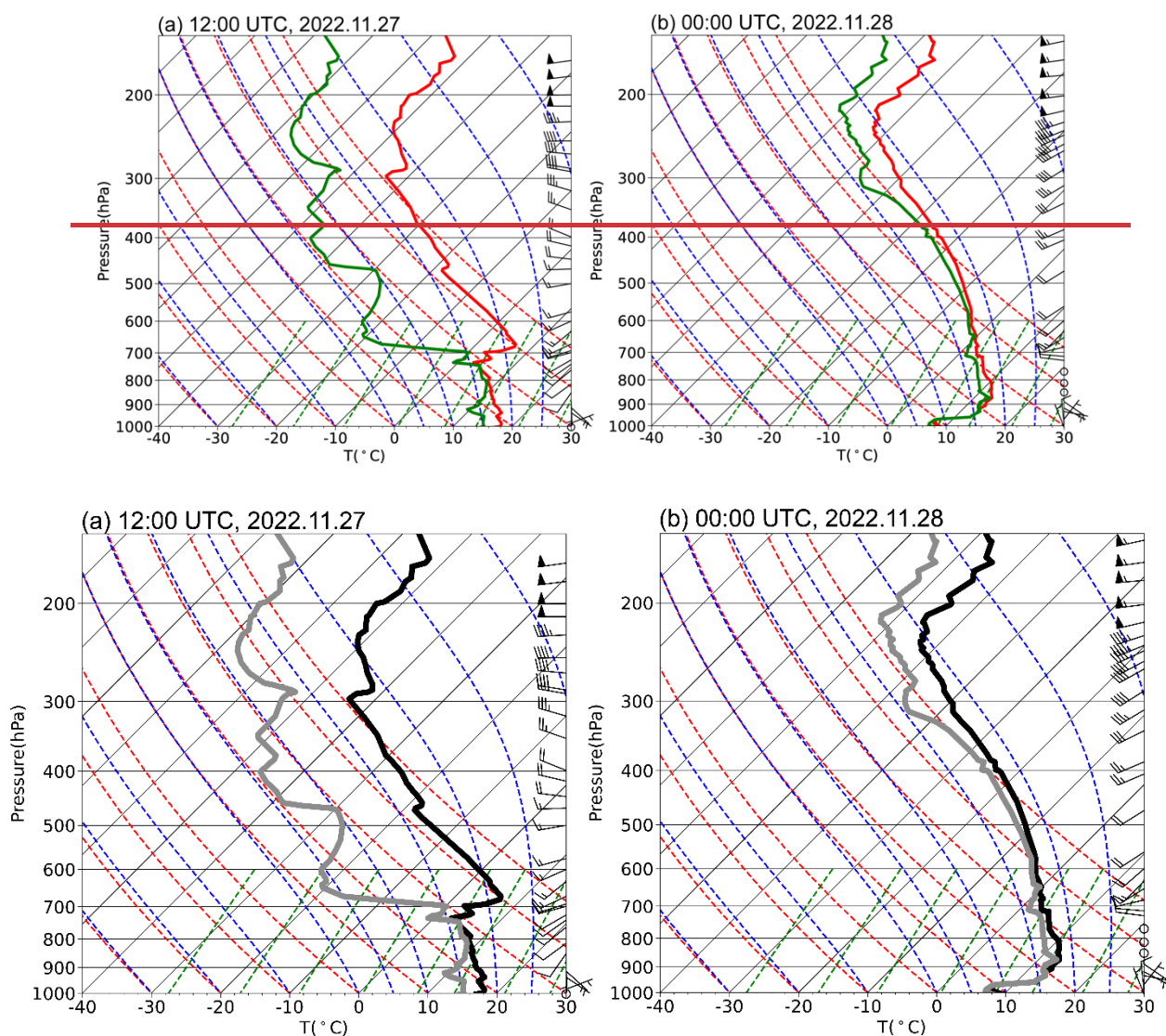
Figure 2: Skew-T log-p diagrams of sounding data from Fuyang at 12:00 UTC on Nov. 27ᵗʰ, and 00:00 UTC on Nov. 28ᵗʰ, 2022. The red profiles indicate the temperature and the green profiles indicate the dew point.
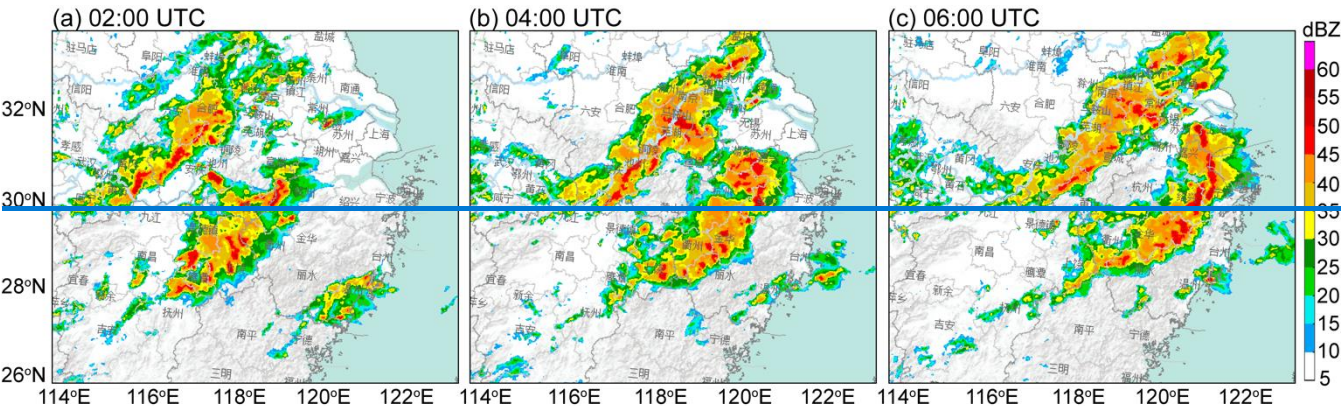
~~Figure 3: Observed radar composite reflectivity at (a) 02:00 UTC, (b) 04:00 UTC, and (c) 06:00 UTC on Nov. 28ᵗʰ, 2022.~~

130

2.2 Model setup and design of numerical experiments

In this simulation, a two-way nested domain is used (Figure 3~~3~~). The outer domain has a grid spacing~~spatial resolution~~ of 9 km. The resolution of the inner domain is 3 km, with 328 × 298 grids. There are 61~~51~~ vertical levels with a top pressure of 50 hPa (~20 km). ~~The 6-hourly NCEP FNL reanalysis data~~The fifth generation ECMWF reanalysis (ERA5), which has a horizontal resolution of 0.25° × 0.25° and an hourly temporal resolution, is used to drive the model and provide the boundary condition. The simulation runs from ~~00~~12:00, Nov. 27ᵗʰ to 12:00, Nov. 28ᵗʰ, with a spin--up time of 12 hours. ~~The fast SBM, in which aerosol and all the hydrometeor species are represented by 33 mass doubling bins, is used to model the cloud microphysics. It is well known that all cloud models could be categorized into bulk parameterization model and bin spectral model depending on the microphysical representation. The bin spectral model does not restrict the particle spectrum to a specific shape, so it is able to show more realistic cloud processes. In Fast SBM model, the ice and snow combined in one size distribution function, as do graupel and hail, and as do cloud droplet and rain. Qu et al. (2020) used 2-D bin spectral model, which included the drop freezing fragmentation and ice-ice collision splintering processes, to do an ideal simulation. It is found that the drop freezing fragmentation process dominates during cloud developing period. Later, the ice-ice collision splintering processes produces large ice crystals. The size distribution of droplet and ice particles have great agreement with observation.~~

The fast spectral bin microphysics scheme (SBM) is used to model the cloud microphysics. Compared to the bulk microphysics scheme, the SBM scheme has the advantage of calculating particle size distributions (PSDs) by solving explicit microphysical equations. It aims to simulate as accurately as possible cloud microphysical processes (Khain et al. 2015). In the fast version of SBM in WRF, the ice and liquid hydrometeor species include cloud droplet/rain, ice/snow, and graupel, each of them is represented by 33 doubling mass bins. It has been demonstrated that SBM performs better than bulk microphysics in modeling

150 cloud microphysics in many previous studies (e.g., Fan et al., 2012; Khain et al. 2015). However, SBM has not been widely used for studying cloud electrification (e.g., Mansell et al., 2005; Shi et al., 2015). Recently, Philips et al. (2020) implemented cloud electrification parameterization in the SBM in a cloud model, and they conducted an idealized simulation of deep convective clouds. The results showed the modeled charge structure and lightning activity are consistent with observations. However, cloud electrification has not been implemented in SBM in WRF for a real case study before.

155

The Kain-Fritsch cumulus scheme is used for the outer domain, while turned off for the inner domain. The other physical choices include the Rapid Radiative Transfer Model for shortwave and longwave radiation (Mlawer et al., 1997), the Revised MM5 surface layer scheme (Jiménez et al., 2012), the Noah land surface model (Tewari et al., 2004), and the Yonsei University planetary boundary layer scheme (Hong et al., 2006).

160
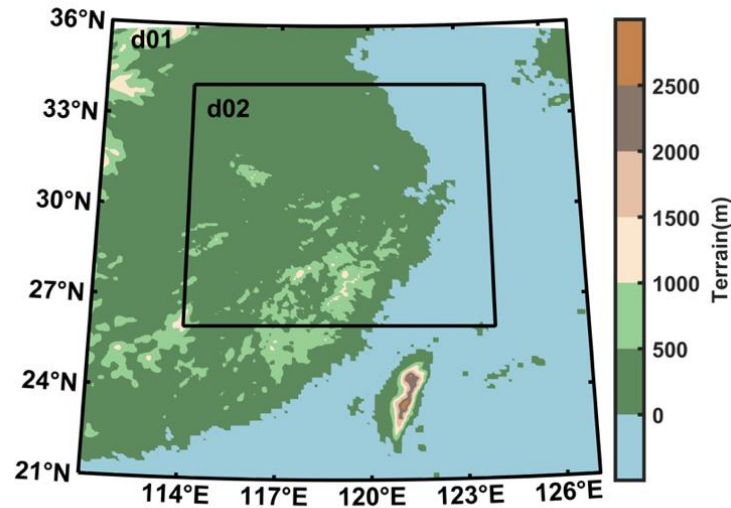
Figure 43: Domains of WRF model simulation.

Parameterizations of fourthree SIP mechanisms are implemented in the SBM: the rime-splintering, ice-ice collisional breakup, and – shattering of freezing drops, and sublimational breakup of ice. The equations of them are detailed in Appendix A. The
165 parametrization parameterization of rime-splintering is developed based on the laboratory experiments made by Hallett and Mossop (1974), which shows an ice splinter is created for every 200 droplets collected by a graupel through riming at -5 °C. This SIP rate decreases as the temperature increases or decreases from -5 °C. At temperatures colder than -8 °C or warmer than -3 °C-. The the rime-splintering is inactive. The parameterization of shattering of freezing drops is also developed based on previous laboratory experiments (King and Fletcher, 1973; Philips et al., 2018). It is a set of functions depending on the
170 particle size and temperature. In this mechanism, either tiny or big ice fragments can be produced when a supercooled liquid drop collides with an ice crystal. The production rate of ice fragments is the highest at -15 °C, but it can also be active at colder

and warmer temperatures (Lauber et al., 2018). The parameterization of ice-ice collisional breakup is developed based on the principle of energy conservation as well as previous laboratory experiments (Takahashi et al., 1995; Yano and Phillips, 2011; Philips et al., 2017). The production rate depends on the density and shape of ice particles, as well as the collision kinetic energy. Deshmukh et al. (2022) proposed a formulation for the number of ice splinters generated during ice sublimation based on laboratory observations. The relative humidity on the ice and the preliminary size of the mother ice particles both govern the number of ice splinters. The formulation is used for dendritic crystals and heavily rimed particles (e.g., graupel). Waman et al. (2022) simulated a squall line with four SIP processes and found that sublimation fragmentation is only active in downdrafts.

Similar to many previous studies (Mansell et al., 2010; Fierro et al., 2013; Guo et al., 2017), we use the parametrization of noninductive charging developed by Saunders and Peck (1998) to simulate the cloud electrification, which is a function of particle terminal velocity, collisional efficiency, temperature and ~~riming~~ rime accretion rate (RAR). This parametrization is supported by a series of laboratory experiments demonstrating that collision between graupel and ice ~~are~~ is the key noninductive charging mechanism (e.g., Brooks et al., 1997; Takahashi and Miyawaki, 2002; Saunders and Peck, 1998; Saunders et al., 2001; Emersic and Saunders, 2010). Some ~~modelling~~ modeling studies showed this parameterization would result in an inverted charge structure (e.g., Mansell et al., 2010; Phillips et al., 2020) in a thunderstorm, while in this study, we will show that with SIP implemented in the model, the charge structure changes from inverted to normal, suggesting correct representation ~~representative~~ of ice generation is vital in ~~modelling~~ modeling the cloud electrification. In addition, a parametrization of inductive charging (Mansell et al., 2005) is implemented in the SBM. The charge transfer occurs during the riming process between polarized supercooled droplets and graupel along grazing trajectories (Moore, 1975). With charge density ~~modelled~~ modeled, the electric field can be calculated based on the Poisson equation, and the discharging is simulated using a bulk model (Fierro et al., 2013). The equations of these parametrizations can be found in Appendix B.

~~Five~~ Six sensitivity experiments are designed to investigate the impacts of different SIP processes on cloud electrification. In the first experiment, none of the SIP parametrizations is used (hereafter noSIP); in the second experiment, only rime-splintering is considered (hereafter RS); in the third experiment, only ice-ice collisional breakup is used (hereafter IC); in the fourth experiment, only shattering of freezing drops is turned on (hereafter SD); in the fifth experiment, only sublimational breakup of ice is applied (hereafter SK); in the last experiment, all the ~~three~~ four SIP mechanisms are considered (hereafter ~~3SIP~~4SIP).

2.3 Description of observation dataset

Radar reflectivity can be used to illustrate the intensity of the storm. The radar data used in this study is a gridded product generated based on 32 S-band radars operated across southeast China. For each radar, the detection radius is 230 km, the range resolution is 250 m and the beamwidth is 1°. The radar finishes a volume scan every 6 minutes consisting of 9 elevation angles

(0.5°, 1.5°, 2.4°, 3.4°, 4.3°, 6.0°, 9.9°, 14.6° and 19.5°). The data recorded by these radars were interpolated into a Cartesian grid with a horizontal resolution of 1 km and vertical resolution of 500 m based on the Cressman technique.

In addition, the lightning location and flash rate are evaluated using observation. The lightning location data is obtained based on the very low frequency (VLF) lightning location network (LLN) in China developed by Nanjing University of Information Science and Technology (Li et al., 2022). VLF-LLN was established in 2021 and has 26 stations distributed across various regions in China. The detection area covers the entire China as well as parts of East and Southeast Asia. The lightning location algorithm is developed based on the time-of-arrival (TOA) method, and the arrival times of each lighting-induced pulse at different stations are obtained by matching the recorded waveforms to the idealized waveforms simulated using the Finite Difference Time-Domain (FDTD) technique. The lightning location error is 1-5 km (Li et al., 2022).

Moreover, the ERA5 reanalysis data is used to investigate the synoptic conditions, the sounding measurement at Fuyang, which is conducted every 12 hours, is used to investigate the thermodynamic conditions, and the brightness temperature (TBB) on the FY2H satellite that is developed in China is used to illustrate the cloud coverage.

3 Results

3.1 Model evaluation~~validation~~

The composite radar reflectivity modelled in the ~~fivesix~~ noSIP and 4SIP numerical experiments is compared with the observation in Figure ~~5~~4. It is within the expectation that the simulated convection inevitably deviates from the observed (fig.4 g-i) to some extent ~~(Fig. 3)~~, but in general, the model well captures the location and scale of the storm. The model also successfully simulates the east propagation of the storm (Fig. ~~5a, f, k~~4a-c). The SIP processes have minor impacts on the macro-properties of the storm, while the intensity can be clearly affected. At 02:00 on Nov. 28th, the noSIP experiment overestimates the composite radar reflectivity, the modelled area with reflectivity greater than 45 dBZ is much larger than observed (Fig. ~~3a and 5a~~ 4a and g). ~~The IC and SK experiments shows little improvement as the radar reflectivity areis also overestimated (Fig. 5c4g and m).~~ With rime splintering or shattering of freezing drops considered, the modelled radar reflectivity is reduced (Figs. ~~5b and d~~4d and j), and ~~Ww~~with all the ~~three~~ four SIP processes implemented, the simulation result is more consistent with the observation (Fig. ~~5e~~ 4 d-f), and is better than the experiments with single SIP process (not shown). Similarly, at 04:00 and 06:00, the radar reflectivity is overestimated in the noSIP experiment (Fig. ~~5f~~4b and c)~~, and can be slightly reduced by the rime splintering or shattering of freezing drop (Figs. 5g and i4e and k). The ice-ice collisional break up and sublimational brekup haves little impact (Fig. 5h4h and n), and the simulation with all the three four SIP processes has the best performance comparing to the observation (Figs. 3b and 5j4q and t). At 06:00, the noSIP experiment again overestimates the intensity of the storm (Fig. 5k4c). The modelled reflectivity can be slightly improved by each of the three SIP processes (Figs. 5l, m and n), and w~~With all the ~~three~~ four SIP processes considered together, the simulation result is more

consistent with the observation than that without SIP, not only for the intensity but also for the shape of the east convective cloud (Figs. ~~3c, 5k and 5o~~ 4d-f). ~~The good performance of WRF in modelling the composite reflectivity and the improvements by SIP provide us confidence to investigate the impacts of SIP on the cloud microphysics and electrification in the cold-season storm.~~

240
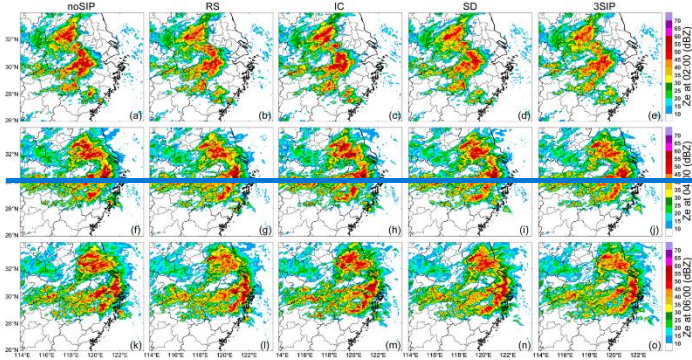
~~Figure 5~~4: (a-c) Composite radar reflectivity modelled in the numerical experiment without any SIP process at 02:00, 04:00 and 06:00 UTC on Nov. 28th, 2022. (d-f) Same as (a-c) but for the experiment in which only rime-splintering is 245 considered. (g-i) Same as (a-c) but for the experiment in which only ice-ice collisional breakup is considered. (j-l) Same as (a-c) but for the experiment in which only shattering of freezing drops is considered. (m-o) Same as (a-c) but for the experiment in which only sublimational breakup is considered. (p-r) Same as (a-c) but for the experiment in which all the four~~three SIP processes are considered. Observed radar composite reflectivity at (s) 02:00 UTC, (t) 04:00 UTC, and (u) 06:00 UTC on Nov. 28th, 2022.~~

250
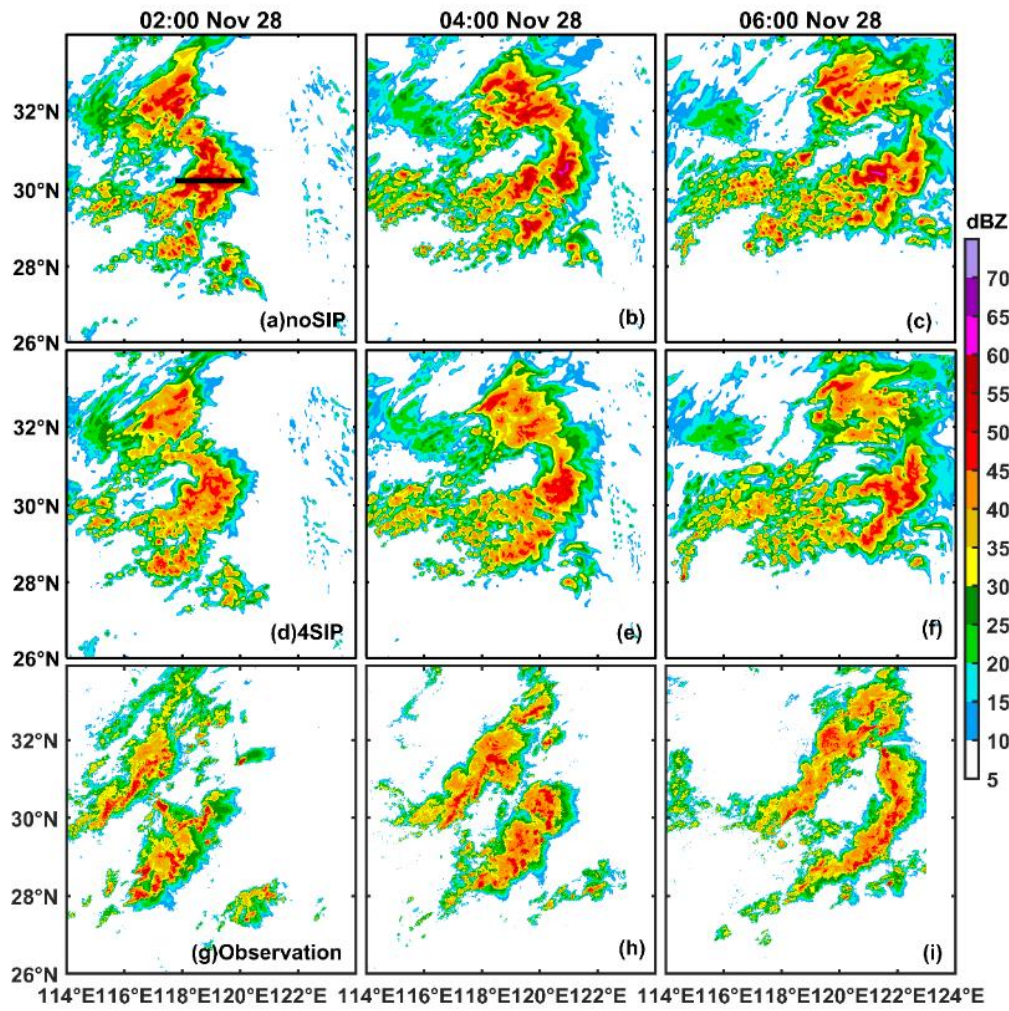
Figure 4: Composite radar reflectivity from (a-c) noSIP, (d-f) 4SIP experiment, and (g-i) observation at 02:00, 04:00, and 06:00, Nov 28th. The black horizontal line in (a) shows where the crorss section used in the following analysiss are from.

255

As discussed above, the composite radar reflectivity in the 4SIP experiment is more consistent with observation. To statistically investigate the difference in the reflectivity at different heights between observation and model simulations, Tthe contoured-frequency-by-altitude diagrams (CFAD) (Fig. 5) of reflectivity are plotted (Fig. 5) to statistically show the difference in the frequency distribution of reflectivity at different heights between observation and model simulations. As seen in Fig. 5, the

260   maximum reflectivity is observed at about 4 km (Fig. 5g-i), which is the height of the melting levels. The modelled maximum reflectivity from the noSIP experiment (Fig. 5a-c) is larger than observed by about 7 dBZ, this is also seen from the map of composite reflectivity in Fig. 4. With SIP implemented, the maximum reflectivity decreases and is more consistent with

observation (Fig. 5d-f). Since the radar reflectivity is calculated for a wavelength of 10 cm, it is more sensitive to particle size, thus, the decreased reflectivity implies smaller particle sizes after SIP processes are used in the model, which will be demonstrated in Section 3.2. The mean reflectivity profiles in both the noSIP and 4SIP experiments are systematically larger than observed as the occurrence frequency of reflectivity greater than 30 dBZ is overestimated, but the 4SIP performs better than noSIP experiment. Note tThe observed reflectivity may beis underestimated at low levels because the lowest elevation angle used in the radar measurement is 0.5° degree and the low-elevation beams are affected by ground clutters. The good performance of WRF in modeling the composite reflectivity and the improvements by SIP provide us the confidence to investigate the impacts of SIP on the cloud microphysics and electrification in the cold-season storm.
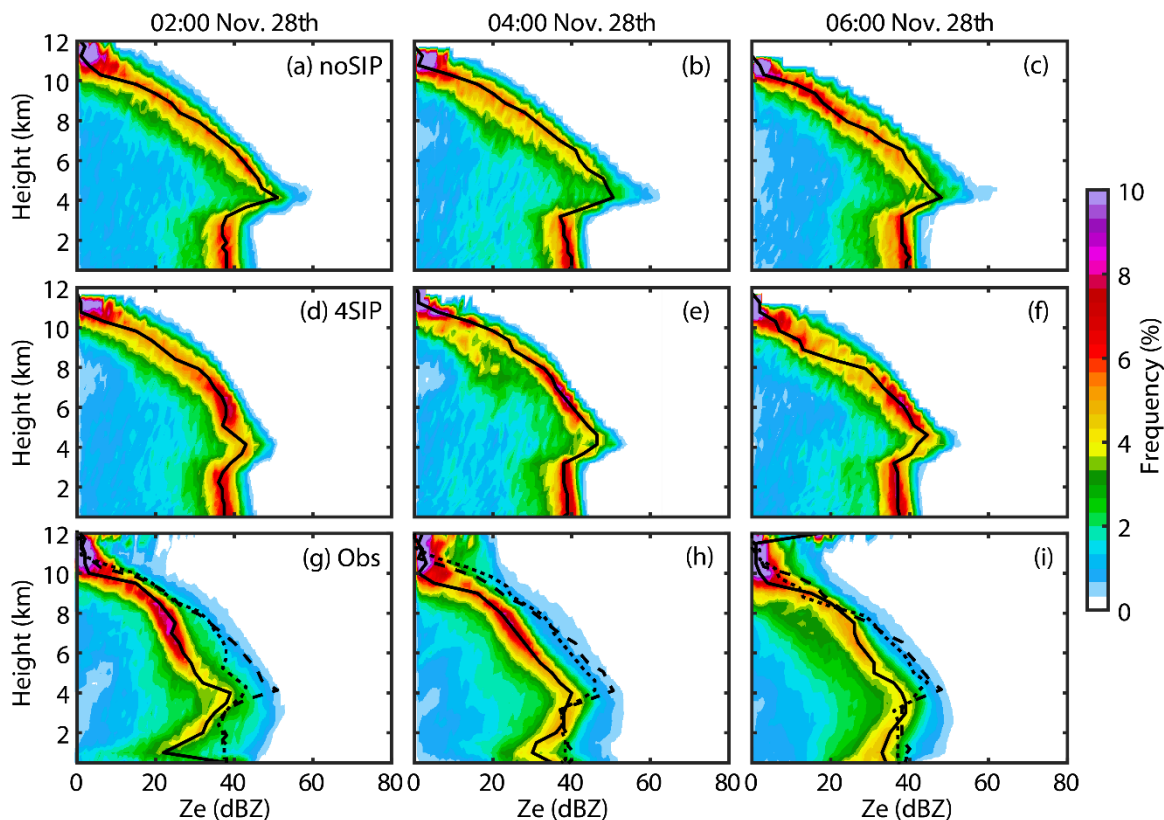
Figure 5: The CFAD of reflectivity from (a-c) noSIP, (d-f) 4SIP experiments and (g-i) radar observation at 02:00, 04:00, and 06:00, Nov 28th. The black lines indicate the profiles of mean reflectivity, and the dashed and whitedotted lines in (g-i) are the mean reflectivity profiles from noSIP and 4SIP experiments.

The flashlightning locations and flash rate from the observation and the numerical experiments are compared in Figure 6. The lighting observational dataset is obtained from the long range lightning location network in China developed by Nanjing University of Information Science and Technology (Li et al., 2022). Since we use a bulk discharge model in simulating the

280 flash, it is within ~~the~~ expectation that there are uncertainties in ~~modelling~~ modeling the lightning frequency. In addition, the lighting occurrence is strongly related to the convective cores, the uncertainty in ~~modelling~~ modeling the flash rate is associated with the uncertainty in ~~modelling~~ modeling the radar reflectivity (Fig. 4 and 5). ~~However, i~~It is seen from Fig. 6a that the lightning locations obtained from the simulations are in agreement with the observations in the southern convection. The simulated lightning ~~clusters~~ are in the low TBB (Brightness Temperature) region, which implies strong convection. ~~Although~~

285 ~~t~~The number of lightning flashes obtained from the simulation in the ~~upper left~~ northern cell ~~cloud~~ (29°E -32°E) is much less than ~~the observation~~observed as WRF failed to simulate the deep convection~~, the simulated lightning in this region are coincide with the region in Fig. 4 where the radar reflectivity is above 40 dBZ.~~ ~~the figure~~The temporal evolution of flash rate in the southern convection is shown in Fig. 6b, it is seen that there is improvement in model~~l~~ing the temporal variation of flash rate by implementing SIP processes. The observation indicates the highest flash rate occurred between 00:00 and 01:00, Nov. 28th.

290 Without any SIP, the flash rate is relatively high before 00:00, Nov. 28th. The ice-ice collisional break-up enhances the flash rate and peaks at about 00:00, Nov. 28th ~~but does not change the temporal variation~~. The flash rate has a similar magnitude in noSIP and IC experiments. The rime-splintering and shattering of freezing drop can improve the simulation as the mode~~l~~led flash rate is ~~reduced before 00:00, Nov. 28th and~~ enhanced after 00:00, Nov. 28th, which is more consistent with observation. The simulated flash rate in SK experiment peaks at 00:00, Nov. 28th~~.~~, with a similar magnitude to that in IC experiment. ~~The~~

295 ~~simulated flash rates for RS and IC are in good agreement with the observations.~~ With all ~~the three~~ four SIP processes implement~~ed~~, ~~the flash rate after 00:00, Nov. 28th is further enhanced, and~~ the model~~l~~ed result is more consistent with the observation than the other experiments after 00:00. ~~It is obvious from Fig. 6a that the lightning locations obtained from the simulations are in agreement with the observations. The simulated lightning clusters in the low TBB (Brightness Temperature) region, which implies strong convection. Although the number of lightning flashes obtained from the simulation in the upper-~~

300 ~~left cloud (29°E -32°E) is much less than the observation, the simulated lightning in this region are coincide with the region in Fig. 4 where the radar reflectivity is above 40 dBZ.~~ Overall, WRF captures the lightning locations and the temporal evolution of flash rate, ~~This~~this provides the basis for further analyzing ~~the~~ cloud electrification.
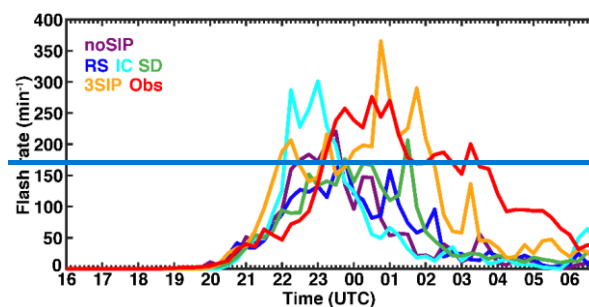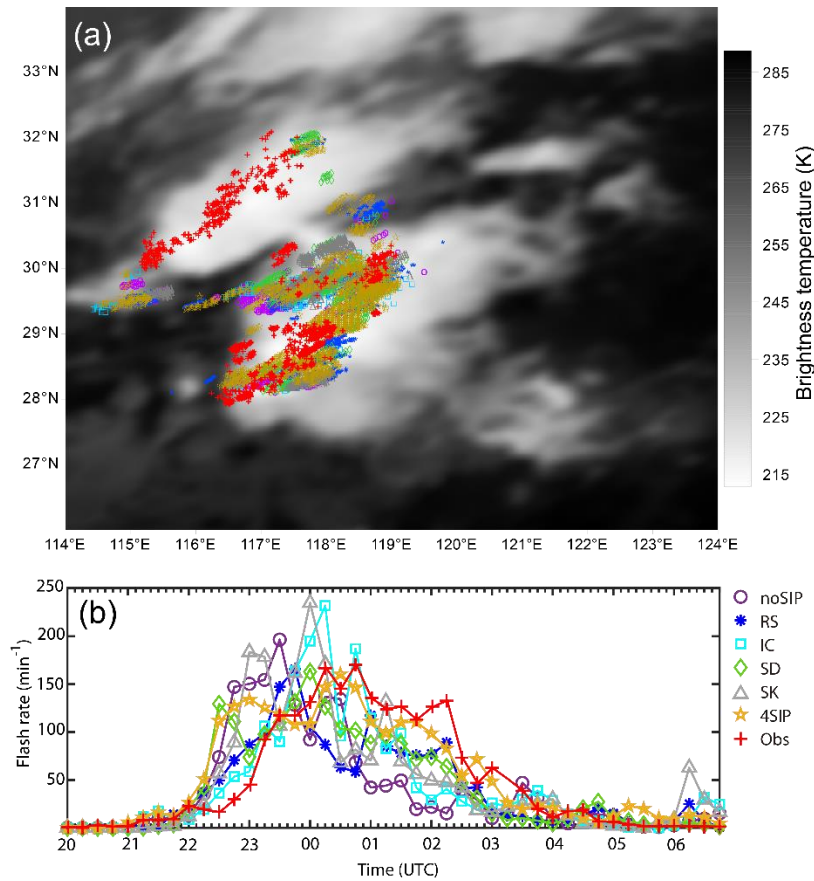
Figure 6: (a) The location of simulated and observed flashes over TBB. (b) The variation of simulated and observed flash rates over time.

3.2 The impact of ice multiplication on cloud microphysics

~~The charge structure in thunderstorm is controlled by the microphysics.~~ The various SIP processes may have different impacts on the cloud microphysics. Figure 7 presents the time-height diagrams of the mixing ratio and number concentration of graupel/hail, ice/snow, rain and cloud water in ~~different~~ noSIP experiment~~s~~. It is seen from the figure that the model~~l~~ed convection was weak before 18:00, Nov. 27th, and only warm rain was present. ~~Between 18:00 and 20:00, the storm rapidly intensified, and the cloud mixing ratio increased substantially.~~ The model~~l~~ed cloud top reached approximately 12 km above the mean sea level (a.m.s.l.), and significant homogeneous ice production took place near -40 °C (Fig. 7f). Between 22:00, Nov. 27th and 02:00, Nov. 28th, the surface rain was relatively strong, and the maximum graupel and rain mixing ratio were about ~~7~~0.11 g kg~~s~~$^{-1}$ and ~~8~~0.13 g kg^{-1}. The snow mixing ratio was ~~lower~~ higher than that of graupel and rain in this period. ~~The strong correlation between the graupel and rain water mixing indicate the melting of graupel had great contribute to the rainfall.~~

The temporal evolution of the rain mixing ratio is consistent with that of snow, suggesting the melting of snow contributes significantly to the rain. After 01:00, Nov. 28th, the cloud top decreased, the surface rain was weakened, and the graupel and liquid water mixing ratio decreased (Fig. 7a and p7a and d), suggesting weakening of convective updraftsion, and this results resulted in the declining flash rate after 01:00 (Fig. 6). However, the snow mixing ratio was higher than that before 02:00, exceeding the mixing ratio of graupel, suggesting melting of snow might be more important to the rainfall in this period. For ice/snow, the mixing ratio peaks between -10°C and -20°C and the concentration peaks above -40°C layer, which indicating that small ice particle clusters at colder region.

The rime-splintering process has a clear enhancing effect on the graupel mixing ratio between 22:00, Nov. 27th and 02:00, Nov. 28th (Fig. 7b), and snow mixing ratio after 02:00, Nov. 28th (Fig. 7g7h). The enhancement of graupel mixing is found mainly above 6 km, while rime-splintering is mainly active between -3 °C and -8 °C, which is below 6 km. This indicates the secondary ice particles might transport to upper levels in the convection. However, the rain mixing ratio decreases due to the SIP by rime-splintering, suggesting less graupel falling out of the cloud, this is probably due to the smaller size of graupel (shown later). However, the mixing ratios of rain and cloud droplets have a slight decrease above 0℃ and -10℃, respectively, indicating the consumption of liquid water by the RS process. The ice-ice collisional breakup also enhances the graupel mixing ratio before 02:00, Nov. 28th and snow mixing ratio after 02:00, Nov. 28th. However, the core area of the mixing ratio for graupel shrinks a lot before 02:00 , Nov. 28th (Fig. 7c). In addition, the rain and cloud water mixing ratio are also enhanced, especially at 4 km (Fig. 7m) and 7 km (Fig. 7r), respectively. The shattering of freezing drops has a minor impact on the graupel mixing ratio (Fig. 7d), however, this does not mean there is few secondary ice particles produced, in fact, the concentration of graupel is enhanced while the size is reduced by this SIP (shown later). The SD process enhances the graupel/hail and ice/snow mixing ratio The snow mixing ratio is enhanced due to shattering of freezing drops after 002:00, Nov. 28th (Fig. 7d and ji) compared to noSIP. In addition,and the rain mixing ratio is reduced afterbefore 02:00, Nov. 28th (Fig. 7pn)., The sublimational breakup has a minor impact on the graupel mixing ratio (Fig. 7e), but enhances the ice/snow mixing ratio after 02:00, Nov. 28th. With all the three four SIP processes implemented, the graupel mixing ratio is markedlyslightly enhanced, and the snow mixing ratio is enhanced as well. However, the rain cloud drop mixing ratio is reduced, resulting slightly weaker surface precipitation above -10℃.
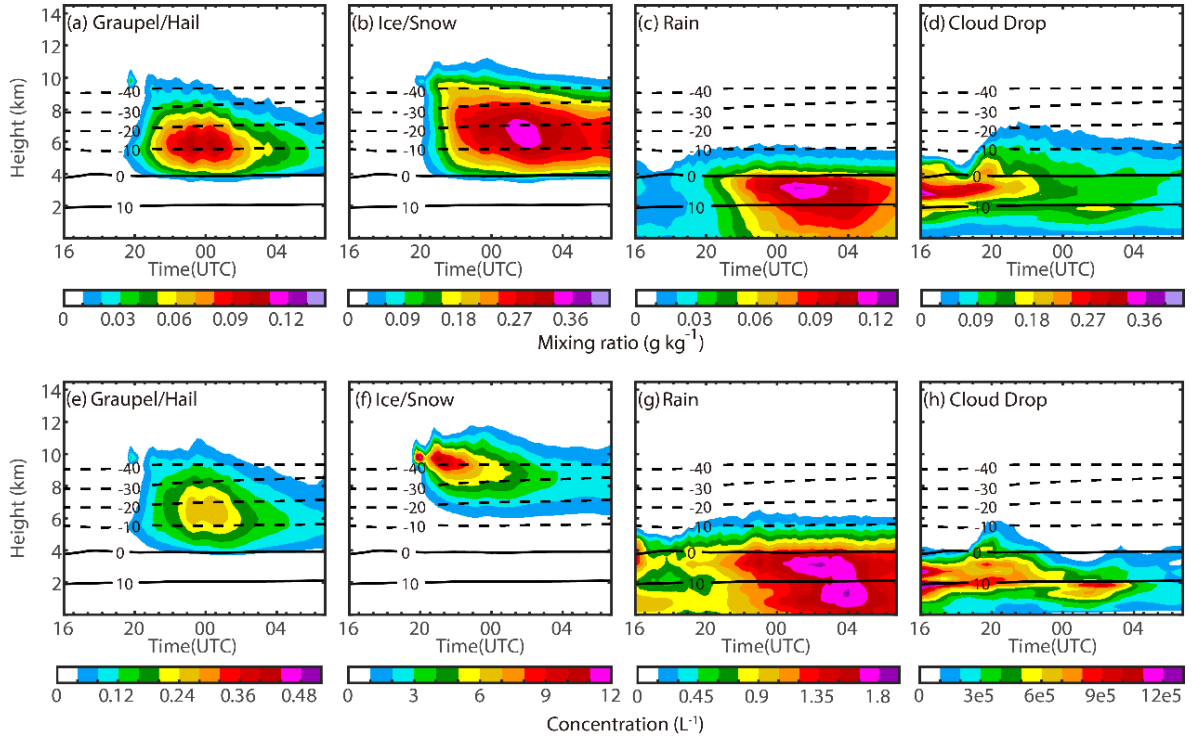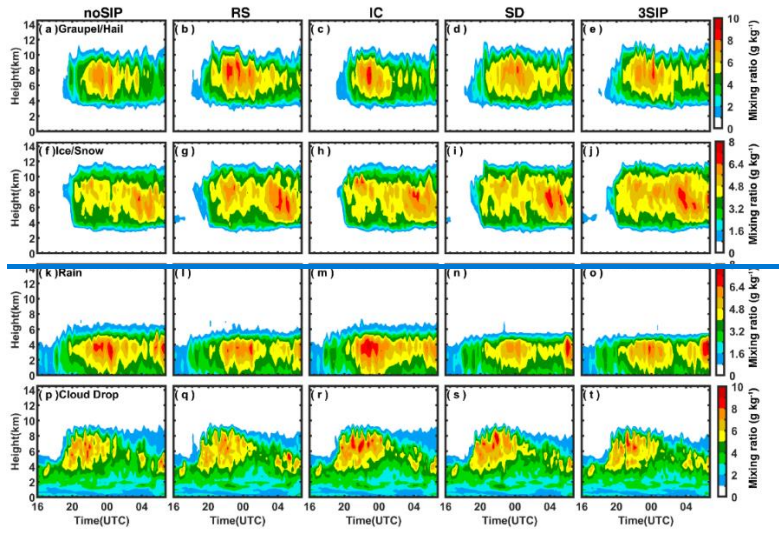
Figure 7: Time-height diagrams of (a, e) graupel/hail, (b, f) ice/snow, (c, g) rain, and (d, h) cloud droplet mixing ratio (upper panels) and concentration (lower panels) in the noSIP experiment.

350

The differences of in the mixing ratios and number concentrations between other experiments with single or four SIP processes and the noSIP experiment are shown in Fig. 8 and 9, respectively. As shown in Fig. 8a and f, the rime-splintering process has

an ~~clear~~ enhancing effect on the graupel and ice/snow mixing ratio ~~between 22:00, Nov. 27th and 04:00, Nov. 28th~~throughout the cloud life cycle, mainly between 0 °C and -20 °C. The maximum increase, which exceeds 0.02 g kg^{-1}, is found between 00:00 and 04:00. However, the mixing ratios of rain and cloud droplets have a ~~great~~ decrease above ~~0°C~~ °C, indicating the consumption of liquid water by the rime-splintering ~~RS~~ process. Thus, less cloud drops may transport vertically to upper levels for freezing. The ~~SD~~shattering of freezing drops also ~~process~~ enhances the graupel/hail and ice/snow mixing ratio ~~after 00:00, Nov. 28th~~ (Fig. 8c and h) compared to noSIP. The enhancement of graupel occurs mainly between 0 °C~~°C~~ and -10 °C~~°C~~ and that of ice/snow occurs at a wider temperature range from ~~-10 °C~~°C to -40 °C~~°C~~. In addition, the rain mixing ratio is reduced ~~after 02:00~~above the freezing level~~, Nov. 28th~~. The ~~IC~~ice-ice collisional breakup and ~~SK~~sublimational breakup of ice ~~processes~~ ~~also~~ enhance the graupel mixing ratio and concentration ~~after 02:00, Nov. 28th. Above -30 °C~~Before 00:00, the ice concentration is high above -30 °C, but they are all small, thus the collisional breakup is insignificant. With all ~~four SIP~~ ~~processes~~ implemented, the graupel ~~mixing ratio is markedly enhanced, and the~~ and snow mixing ratio ~~is~~are enhanced throughout the cloud life cycle ~~as well. As shown in Fig. 9a and f, t~~The ~~RS~~rime-splintering and shattering of freezing drops are responsible for the enhancement of~~process greatly enhances the~~ graupel and ice concentrations ~~of graupel between~~ 0 and -30 °C (Fig. 9e and j) ~~as well as ice/snow between 0 and -20°C.~~, and ~~t~~The ~~SD~~ice-ice collisional breakup, shattering of freezing drops, and sublimational breakup of ice are ~~process~~ ~~enhance the graupel concentration between 0 and -20°C after 22:00, Nov. 27th.~~are responsible for the ice concentration enhancement above -40 °C (Fig. 9j).
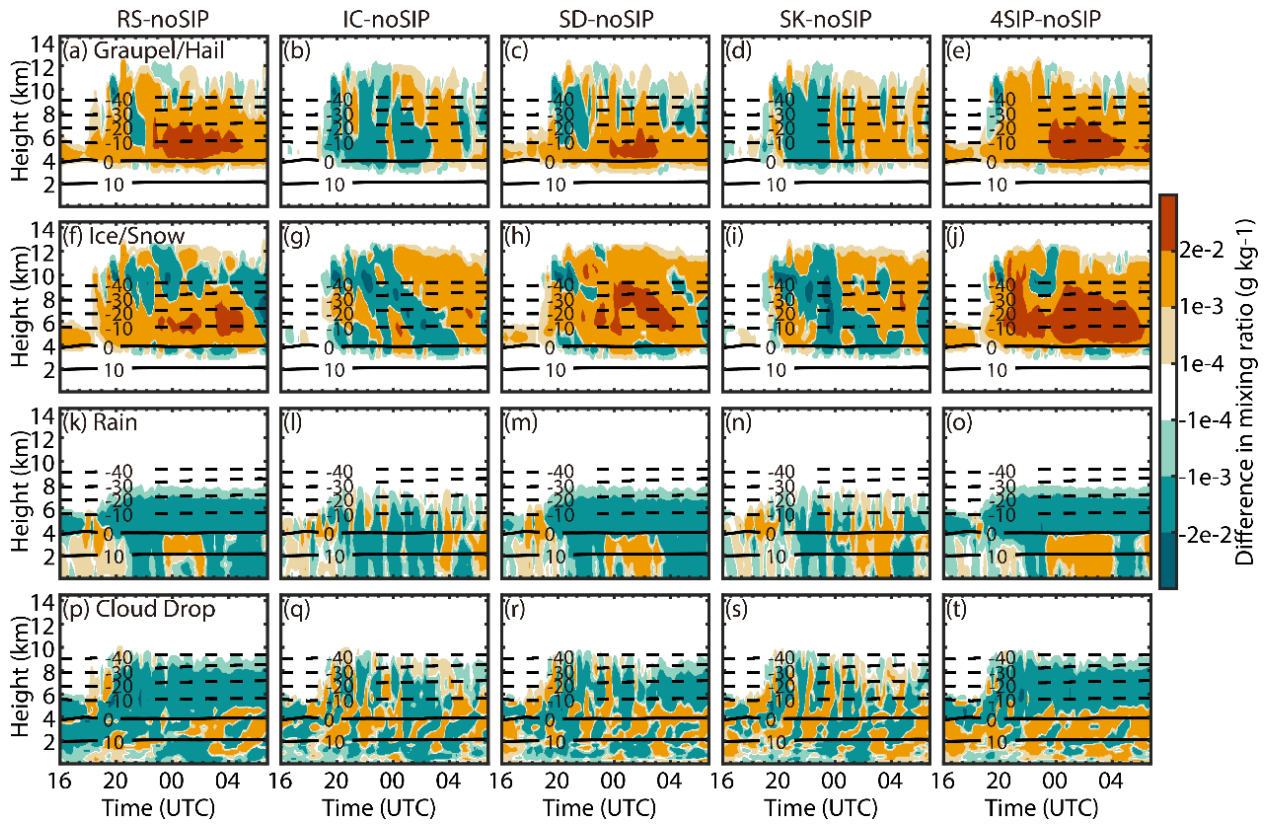
Figure 8: Differences in the mixing ratio of different hydrometeors between the experiments with SIP and those without SIP. (a, f, k, p) experiment with rime-splintering, (b, g, l, q), experiment with ice-ice collisional breakup (c, h, m, r) experiment with shattering of freezing drops, (d, i, n, s) experiment with ice breakup during sublimation, and (e, j, o, t) experiment with four SIP processes.
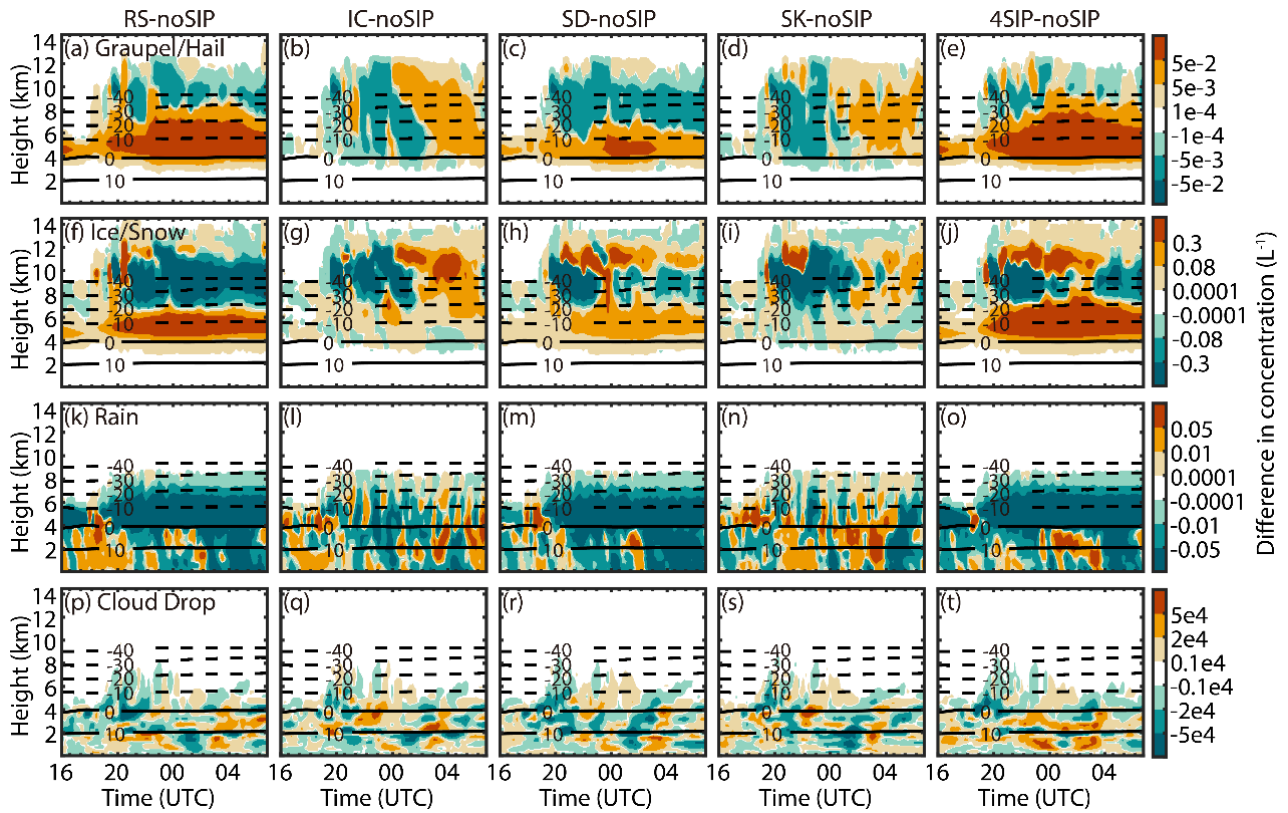
Figure 9: The same as Fig. 8, but for number concentration.

Figure 8 show the distribution of number concentration. The number concentrations of graupel/hail and ice/snow peaks at
380 about 7km and 9km, respectively (Fig. 8 a and g). As shown in fig. 8h, a significant increase in ice/snow particle number
concentration is observed in the region of approximately −10 °C to 0 °C, which coincides with the temperature region where
the RS process is active. However, the peak region between −40 °C and −30 °C seems to decay. Besides, the RS process also
results in the peak graupel/hail number concertation increasing from 0.06 L^{-1} to 0.12 L^{-1} and the peak region falling from about
7km to 5km, which means that the riming process is intense in the −10 °C to 0 °C region. For IC process (Fig. 8 c and i), there
385 is a slight decrease in the number concentration of graupel/hail and ice/snow before 02:00, Nov. 28th. The fall of the core
region for graupel/hail number concentration and the decrease in the ice/snow particle number concentration at about 9 km
also occur in the SD process. The SK process has almost the same graupel/hail number concentration as noSIP simulation.
With four SIP processes considered, the graupel/hail number concentration increases from 0.06 L^{-1} to 0.14 L^{-1}. The ice/snow
number concentration between −20 °C and 0 °C increases from 0.1 L^{-1} to 0.5 L^{-1}. However, for 4SIP simulation, the rain number
390 concentration above 0 °C decreases. The ice/snow concentration is enhanced by rime splintering and shattering of freezing
drops and the maximum increment is more than 0.005 /L. If all the four SIP processes work together, the ice/snow concentration

The enhanced graupel/hail and ice concentrations and decreased composite reflectivity by SIP processes imply decreased diameters of graupel/hail and ice/snow (Fig. 10). Figure 10 shows the profiles of the sizes of graupel/hail and ice/snow. At temperatures higherwarmer than -20 °C, the graupel/hail and ice/snow sizes obtained from the RS and 4SIP experimenttal simulations decrease significantlyby about 0.2 mm and 0.6 mm, respectively., which coincides with Figs. 8a, e and Fig. 9a, e. In the region colder than -20 °C, there is a slight increase in graupel size for both two experiments, but the ice concentration remains similar after implementing SIP. This can be inferred from Figs. 8 and Fig. 9, which shows an increase in the graupel mixing ratio and a decrease in the graupel number concentration in the region colder than -20 °C. The graupel and snow sizes are also reduced due to shattering of freezing drops, and its impact increases with decreasing height. On average, the ice-ice collisional breakup and sublimational breakup of ice has minor impacts on the graupel and ice size, which is a result of cancellation of regions with positive and negative impacts.
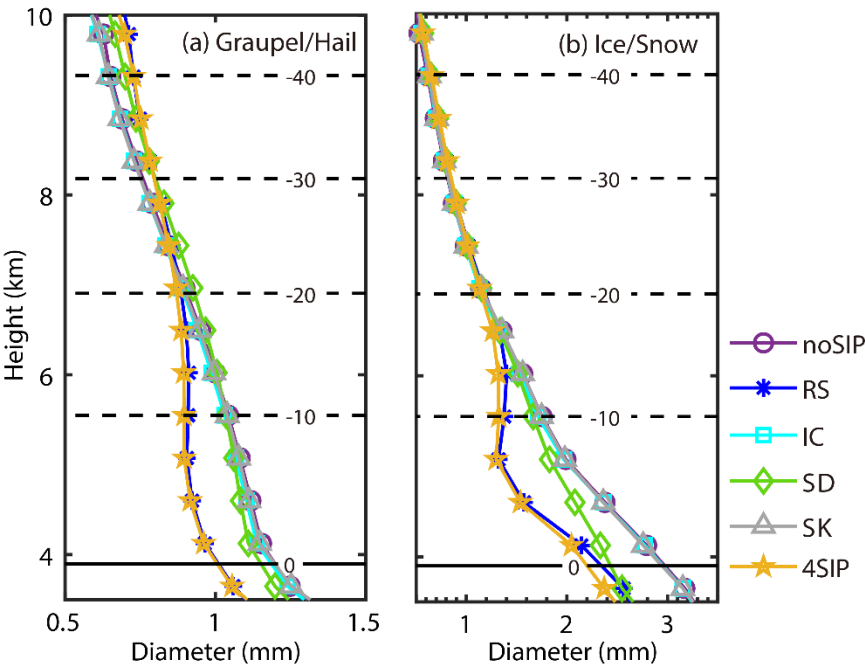
Figure 10: Profiles of the dDiameters of (a) graupel and (b) ice/snow.

With respect toBased on the above discussion on analysis of the average microphysical properties, it is found that RSthe rime-splintering and SD processes have a greaterprocess has the greatest impact on cloud microphysics than IC and RS processes. The regional average data may cause the loss of detailsmicrophysics. However, in some areas, the other SIP processes could be important, thereforeAs seen from the cross sections of mixing ratio and number concentration of graupel, snow, and rain hydrometeorsare shown in Fig. 11 and 12, the graupel and ice concentrations are enhanced in the IC experiment. However, this is not simply due to the secondary ice produced by ice-ice collision, it is the stronger homogenous droplet freezing in IC experiment contributes significantly to the ice production near -40 °C. The composite impact of the four SIP process is not simply the sum up of them, and may be weaker than the impact of single SIP process., These figures help understand the spatial distribution of microphysics. It is seen that though the impacts of the ice-ice collisional breakup and sublimational breakup are small on average (which is seen in the time-height diagrams), both two process can significantly enhance graupel or ice concentration in some areas (Fig. 12c, i, e, k). It is difficult to tell which SIP process has the most significant impact on cloud microphysics simply based on these cross sections, as the composite impact of the four SIP processes is not simply a sum of them (Fig. 11f, l, r, x).
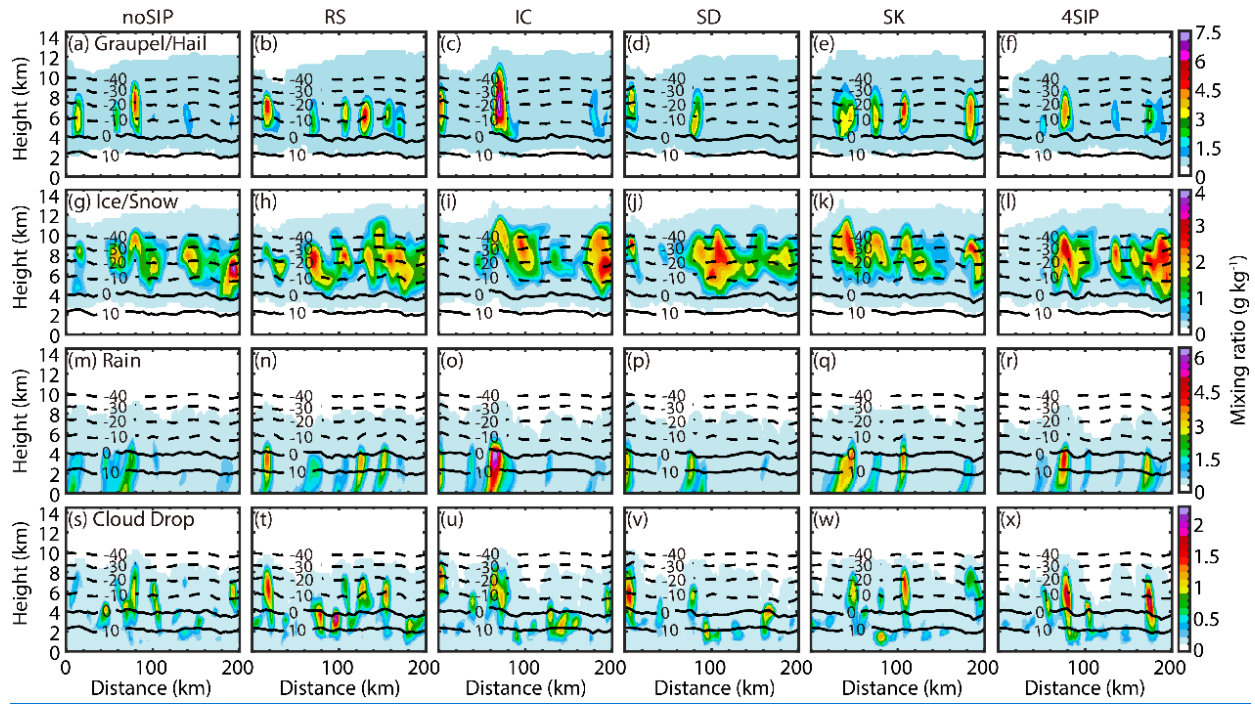
Figure 11: Cross sections of the modelled mixing ratio for (a)-(f) graupel/hail, (g)-(l) snow/ice, (m)-(r) rain, and (s)-(x) cloud droplet along the black line in Fig. 5a at 01:00 Nov. 28th.
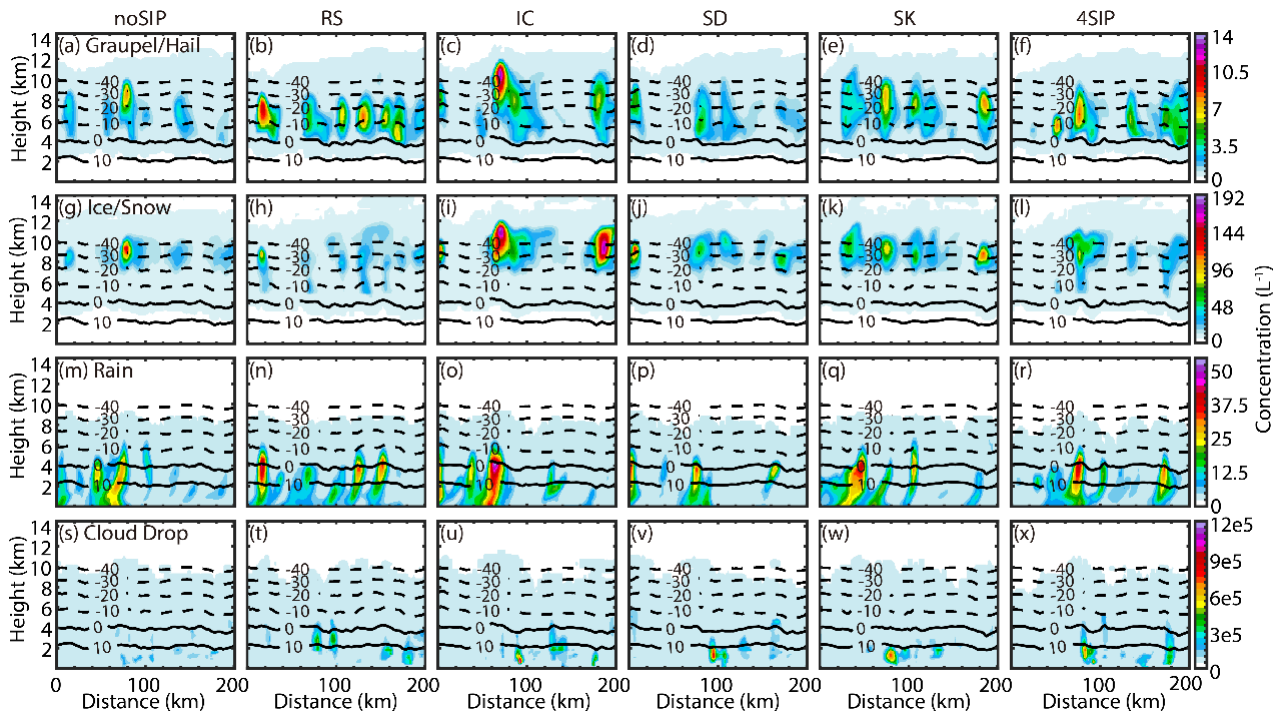
Figure 12. The same as Fig.11 but for concentration.

To understand the relatively importance of the four SIP processes, t~~T~~he ice production rate of the ~~four SIP processes~~m in the 4SIP experiment is illustrated in Fig. 13, which well presents that the magnitudes and locations of intense~~, as the locations where~~ secondary ice productions ~~is intense~~ are different among the four processes. As seen in Fig. 13, the rime-splintering and drop shattering produce significant secondary ice in the core of clouds, where the graupel and rain mixing ratio are high, while the sublimational breakup of ice/snow is more intense near cloud edges or regions with relatively low reflectivity, probably because of the entrainment mixing and regional downdrafts. Ice-ice collisional breakup is more intense in regions with high ice/snow concentrations (Fig. 12~~ef, i~~l). The ice production rate by rime-splintering is the highest, and that by the sublimational ice breakup is the lowest, this substantial difference in the magnitude of the ice production rate is also true after averaging the entire cloud region, and it explains why the rime-splintering process has the most significant impact on the cloud microphysics on average.
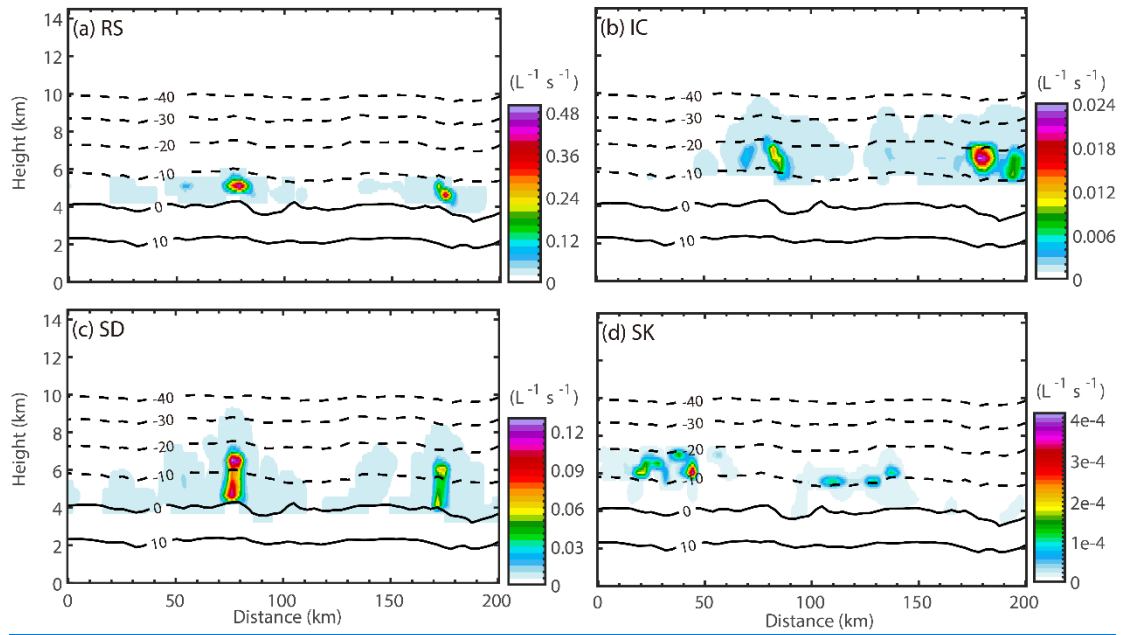
Figure 13: Cross section of the production rates of secondary ice resulting from four SIP mechanisms at 01:00 Nov. 28th. (a) experiment with rime-splintering, (b) experiment with ice-ice collisional breakup, (c) experiment with shattering of freezing drops, (d) experiment with sublimational breakup.

3.~~2~~ 3 The impact of ice multiplication on cloud electrification

The enhanced graupel and ice mixing ratio and concentration ~~would~~ may affect the charging rate by enhancing the graupel-ice collision and riming process. Figure ~~9~~ 14 shows the average noninductive and inductive charging rate obtained from the six~~five~~ numerical experiments. Note the charging rate averaged over the ~~model domain~~ cloud area is very small, the maximum charging rate (not shown) is more than 4 orders of magnitudes larger than the average value, but the pattern is similar, thus providing the same conclusions. It is seen from the figure that the cloud electrification starts at about 19:00, Nov. 27th. Without any SIP considered in the model, the noninductive charging rate has an obvious separation at -20 °C, with negative charging above this level, and positive charging below (Fig. ~~9~~14a). The magnitude of the upper-level negative charging rate is slightly larger than the positive charging rate.

However, with rime-splintering included, the positive charging rate below 7 km is clearly enhanced (Fig. ~~9c~~14~~e~~b), as rime-splintering is efficient at relatively warm temperature. In fact, rime-splintering process is mainly efficient between -3 °C and -8 °C, but the secondary ice can transport to higher levels in convection. The shattering of freezing drops also enhances the positive charging rate below 7 km (Fig. ~~9g~~14d)~~, this SIP is more efficient than the rime-splintering at temperatures colder than~~

‑8 °C. ~~The ice‑ice collisional breakup can slightly~~ ~~decrease~~enhance ~~the graupel and ice mixing ratio, but its impact is too weak to modify the charging rate in this case (Fig. 9e). The same situation is also shown in SK process (Fig. 10i).~~ The ~~IC~~ice‑ice collisional breakup and ~~SK~~sublimational breakup of ice ~~processes~~ only have ~~little~~weak impacts on noninductive charging rate.

465 With all the ~~four~~three SIP processes included, the low-level positive noninductive charging rate on graupel is ~~clearly~~ enhanced (Fig. ~~9i~~14k), mainly due to the composite impact of rime-splintering and shattering of freezing drops. The magnitude of upper-level negative noninductive charging rate remains similar compared to that without SIP.

The inductive charging rate is a few times smaller than the noninductive charging rate, but cannot be neglected. The rime-

470 splintering and shattering of freezing drops result in very different structures of the inductive charging rate compared to that without SIP (Fig. ~~9b~~14~~b~~g, ~~dh~~, ~~hj~~). The upper-level negative charging on graupel in noSIP experiment is changed to positive, this implies that the total charge structure may be inverted above 6 km due to these two SIP processes, which will be demonstrated later. In contrast, the distributions of the inductive charging rate ~~for~~in the IC and SK ~~processes~~experiments ~~is~~are ~~almost the same as for~~similar to that in the noSIP simulation. With all the ~~three~~ four SIP processes implemented, the inductive

475 charging on graupel is positive at most of the levels (Fig. ~~9j~~14l), while at about -10 °C, the graupel sometimes gets negative charging. This indicates an opposite sign of vertical electric field; thus, positive charge (or relatively weak negative charge) regions are present at some locations at this level.

480 ~~The modified charging rate by SIP results in changes in the structure of charge density carried by different hydrometeors, especially the graupel and ice. As shown in Figure 1~~1~~0, the average charge density carried by graupel/hail is negative at all levels if not considering the SIP. Although the graupel gets positive charge by colliding with ice below 8 km (Fig. 1~~0~~9a), the graupel falling from upper levels brings negative charge to the lower levels. In addition, the graupel may get negative charge through riming (Fig. 1~~0~~9b). Therefore, the composite negative charge on graupel exceeds the positive charge generated by noninductive charging. The ice/snow mainly carries positive charge below 10 km (Fig. 11g~~1~~0f), indicating significant~~

485 ~~sedimentation of snow crystals generated between 8 km and 10 km, and the positive charge carried by these falling snow crystals exceeds the negative charge transferred to snow through noninductive charging below 8 km. The enhanced noninductive charging rate by rime-splintering resulting in positive (negative) charge on graupel (snow) below 7 km (Fig. 10 b and g11b and h), indicating the positive charge on graupel gained from charge separation at this level exceeds the negative charge carried by the falling graupel. In addition, the upper-level negative charge on graupel is weakened due to the positive~~

490 ~~inductive charging (Fig. 1~~0~~9d). The shattering of freezing drops has similar impact on the charge structure compared to rime-splintering, but the region with the most enhancement of the positive charge on graupel is slightly higher in SD experiment than in RS experiment (Fig. 10d and i), because the rime-splintering is active between -3 °C and -8 °C, while shattering of freezing drops is also active at colder temperatures. Above 7 km, the negative charge carried by graupel is weakened, probably due to the enhanced positively inductive charging (Fig. 1~~0~~9d and h). The composite effect of rime-splintering and shattering~~
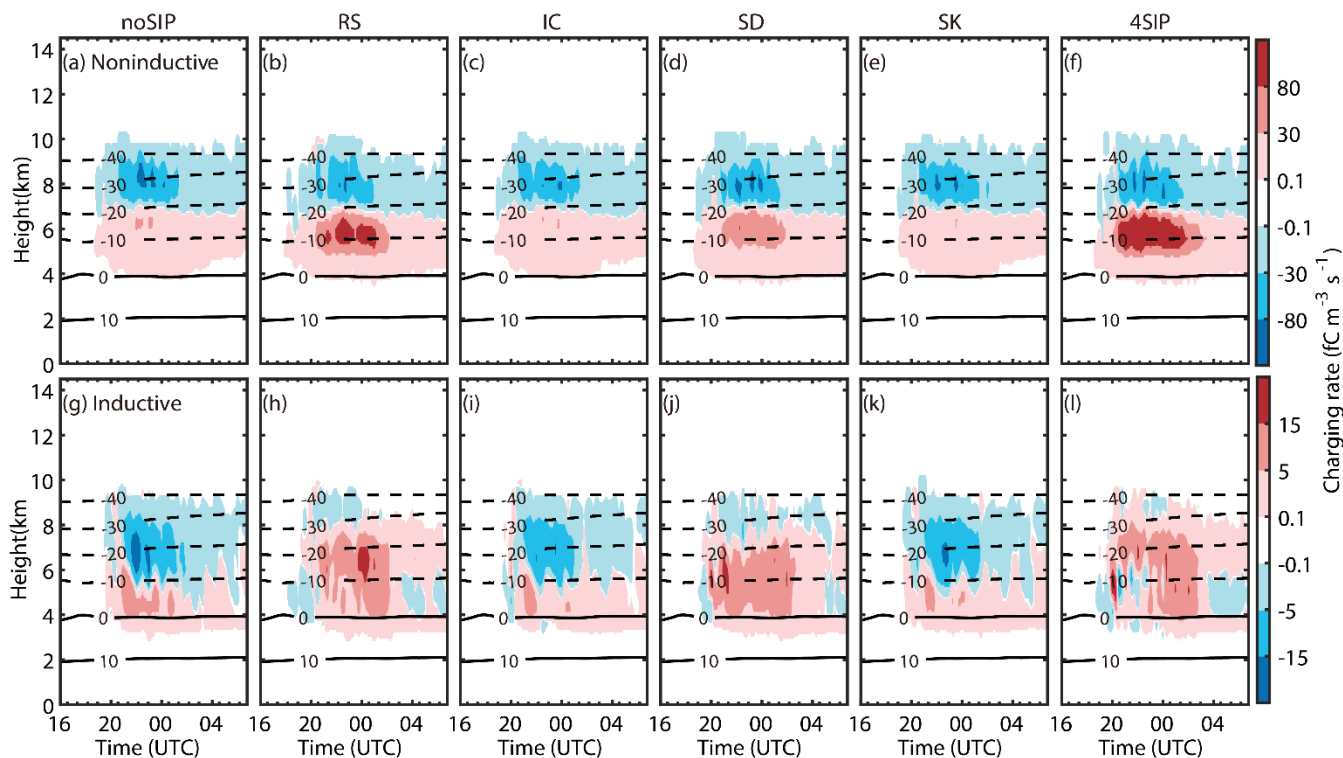
Figure ~~9~~ 14: Time-height diagrams of the charging rate on graupel through noninductive (left panels) and inductive (right panels) charging from the ~~five~~ six experiments. (a, b) experiment without SIP, (c, d) experiment with rime-splintering, (e, f) experiment with ice-ice collisional breakup, (g, h) experiment with shattering of freezing drops, (i, j) experiment with sublimational breakup and (~~i, j~~k, l) experiment with ~~three~~ four SIP processes. The black contours are the isotherms.

The modified charging rate by SIP results in changes in the structure of charge density carried by different hydrometeors, especially the graupel and ice. As shown in Figure 15, the average charge density carried by graupel/hail is negative at all levels if not considering the SIP. Although the graupel gets positive charge by colliding with ice below 8 km (Fig. 14a), the graupel falling from upper levels brings negative charge to the lower levels, this will be discussed in more detail in Figs. 16 and 17. In addition, the graupel may get negative charge through riming between -20 °C and -10 °C. Therefore, the composite negative charge on graupel exceeds the positive charge generated by noninductive charging. The ice/snow mainly carries positive charge below 10 km (Fig. 14g), indicating significant sedimentation of snow crystals generated between 8 km and 10 km, and the positive charge carried by these falling snow crystals exceeds the negative charge transferred to snow through noninductive charging below 8 km. The enhanced noninductive charging rate by rime-splintering resulting in positive (negative)

charge on graupel (snow) below 7 km (Fig. 15b and h), indicating the positive charge on graupel gained from charge separation at this level exceeds the negative charge carried by the falling graupel. Above 7 km, the negative charge carried by graupel is weakened, probably due to the enhanced positively inductive charging (Fig. 14db and h). The ice-ice collisional breakup and sublimational breakup of ice enhance ice concentration after 01:00 (Fig. 9), but tThe relatively low graupel and droplet concentrations after 01:00 prevent the intensification of charge separation, this explains why collision between ice crystals has a weaker impact than rime-splintering and drop shattering on cloud electrification in this case.
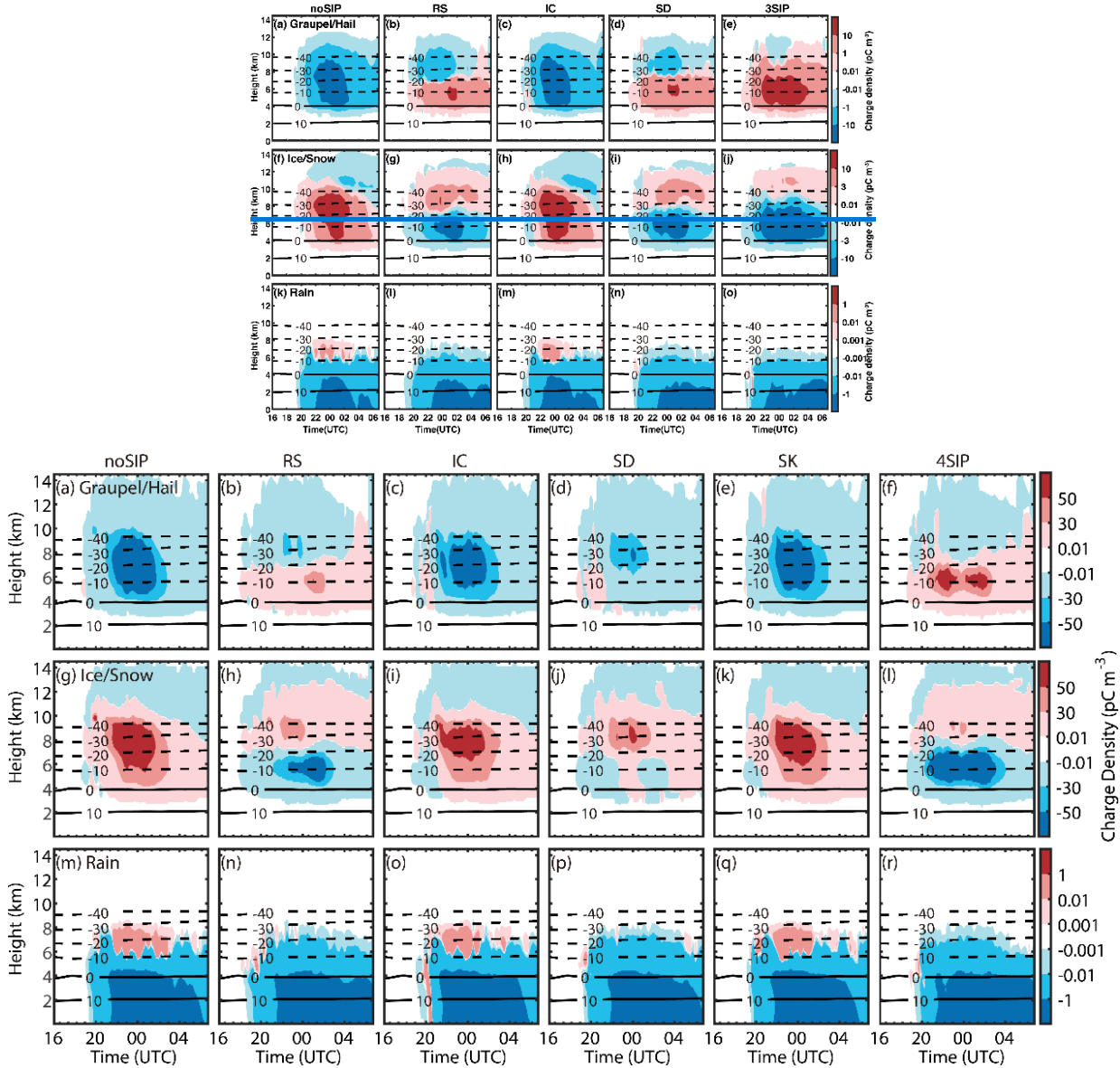
Figure ~~110~~ 15: Time-height diagrams of the charge density carried by (a-~~e~~f) graupel/hail, (~~d-j~~g-l) ice/snow, and (~~k-o~~m-r) rain from the ~~five~~ six simulations. (a, ~~f~~g, ~~k~~m) experiment without SIP, (b, ~~g~~h, ~~l~~n) experiment with rime-splintering, (c, ~~h~~i, ~~m~~o) experiment with ice-ice collisional breakup, (d, ~~i~~j, ~~n~~p) experiment with shattering of freezing drops, (e, k, q) experiment with sublimational breakup, and (~~e~~f, ~~l~~j, ~~r~~o) experiment with ~~three~~ four SIP processes. The black contours are the isotherms.

To better understand the different vertical distributions of charge density and charging rate, t~~T~~he cross--sections of the modeled graupel charge density and noninductive charging rate ~~for~~from the six experiments are shown in Fig. 16. The charge density of graupel (Fig.16a-f) are in agreement with the distribution of graupel (Fig.12a-f) and ice/snow concentrations (Fig.12g-~~i~~l), which reveals the importance of the ice-phase particle number concentration for cloud electrification. The cross--sections of noninductive charging rate exhibit a distribution of upper negative and lower positive (Fig. 16g-l). ~~As shown in Fig. 16g, during charge separation~~indicating~~,~~ i.e., the upper graupel particles get negative charges and the lower graupel particles get positive charges. Since a threshold of RAR>0.1 g m^{-3} s^{-1} is required to trigger charge separation, charging only occurs in areas with relatively high graupel concentration~~-~~, while fall of graupel with negative charge is found in more areas. If the magnitude of the low-level positive charging rate is small, the average charge density would be negative, while if the magnitude of the low-level positive charging rate is enhanced by SIP, the average low-level charge density on graupel is positive. ~~The upper negatively charged graupel particles fall into the positively charged region and since the negative charge is greater than the positive charge, the lower region also becomes negatively charged (Fig. 16 a). This explains why, in the noSIP experiment, the noninduced charging rate is top negative and bottom positive, whereas the graupel is mono-negative charged. This could certainly explain the RS and 4SIP experiments in which the graupel charge exhibits a top negative and bottom positive structure.~~
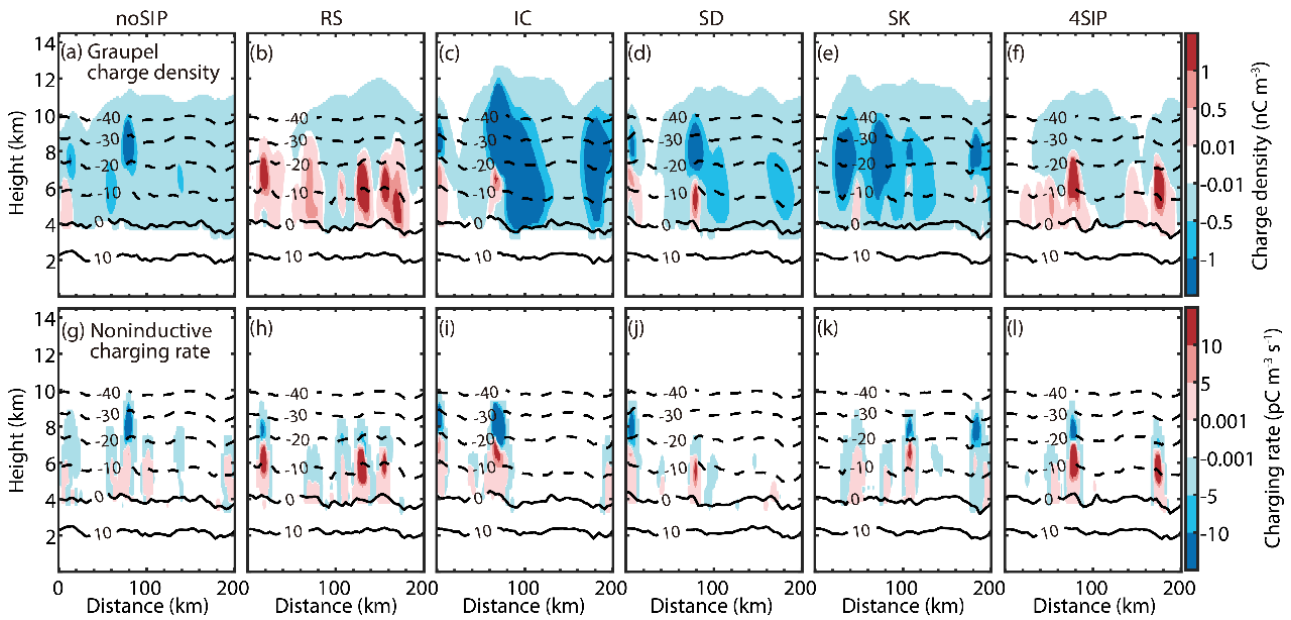
Figure 16. Cross sections of the modeled (a-f) graupel charge density and (g-l) noninductive charging rate.

~~In order to understand the importance of noninductive charging~~The above analysis is valid if considering noninductive charging only~~,~~ as indicated by a sensitivity test in which only ~~non~~inductive electrification is ~~considered~~turned off ~~is made in this paper and the results are shown in Fig. 17~~. Figure 17 shows the graupel charge density, noninductive charging rate, and the fraction of area with charge separation occurring. In the noSIP experiment, the graupel charge density is negative, while the noninductive charging rate has a ~~d~~bipol~~ear~~ structure. The magnitude of the low-level positive charging rate is much smaller than the high-level negative charging rate. This result is the same as that shown in Fig. 14 and Fig. 15, in which both noninductive and inductive charging are considered. Therefore, it is evident that the charge density is mainly controlled by noninductive charging. ~~The different structures of the average charge density and charging rate indicate some crucial information is cancelled by averaging. Since a threshold of RAR>0.1 g m⁻³ s⁻¹ is required to trigger charge separation,~~ ~~e~~Although positive charging takes place at temperatures warmer than -20 °C, its magnitude is small and ~~charging~~ ~~takes place~~ only occurs in a small fraction of the cloud area (Fig. 17e and f), thus, the average charge density on graupel is negative. With rime-splintering implemented, the low-level positive charging is substantially enhanced, and the average charge density on graupel is positive at temperatures warmer than -20 °C. ~~This is more intuitive in the cross sections shown in Fig. 16. Charging only occurs in areas with relatively high graupel concentration (Figs. 16g-l and 12), while fall of graupel with negative charge is found in more areas. If the magnitude of the low-level positive charging rate is small, the average charge density would be negative, while if the magnitude of the low-level positive charging rate is enhanced by SIP, the average low-level charge density on graupel is positive. This information is added to the paper.~~

565
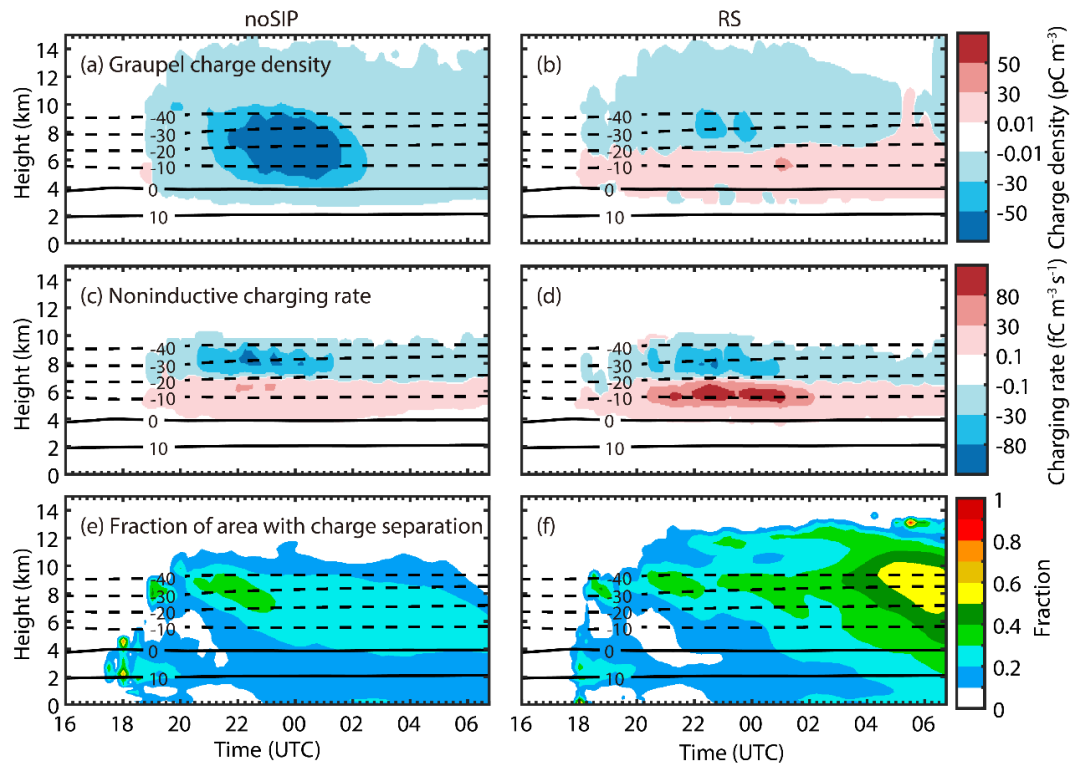
Figure 17: Time height diagrams of (a, b) graupel charge density, (c, d) noninductive charging rate, and (e, f) fraction of area with charge separation occurring in noSIP and RS experiments with only noninductive charging used.

The time-height evolution of the total charge density obtained from different simulations is shown in Figure ~~11~~18. In the

570 experiment without any SIP (Fig. ~~11a~~18a), the storm has an inverted tripole structure with a positive charge region at 7-10 km, and an upper and a lower negative charge region. The positive charge region weakened after 02:00, Nov.28th due to the lower positive charging rate (Fig. ~~9a~~14a). ~~The ice-ice collisional breakup may slightly enhance the positive charge region (Fig. 11c), but this impact is minor as its impact on the ice microphysics and charging rate are weak (Figs. 7 and 9e).~~ With ~~either~~ rime-splintering ~~or shattering of freezing drops~~ implemented, the charge density changes to a dipole structure on average (~~Fig. 12~~11b

575 ~~and d~~Fig.18 b). ~~The main p~~Positive charge dominated above ~~7~~8 km, while main negative charge dominated below ~~7~~8 km. A weak negative charge layer is present at cloud top~~, though the magnitude is small~~. This indicates the magnitude of charge carried by ice/snow is ~~slightly~~ larger than ~~the~~ that carried by graupel/hail (~~Fig. 10b, d, g, and i~~11b, d, h and jFig.15 b and h). With the ~~three~~ four SIP processes included, the charge structure is dipole as well, suggesting the rime-splintering ~~and shattering of freezing drops~~ dominates the SIP effect. In addition, it is seen that the charge reversal level shifts upwards by about 1 km

580 and the magnitude of the upper-level positive charge density is ~~lower~~ greater compared to that in RS and SD experiments due to the composite effect of the SIP processes.
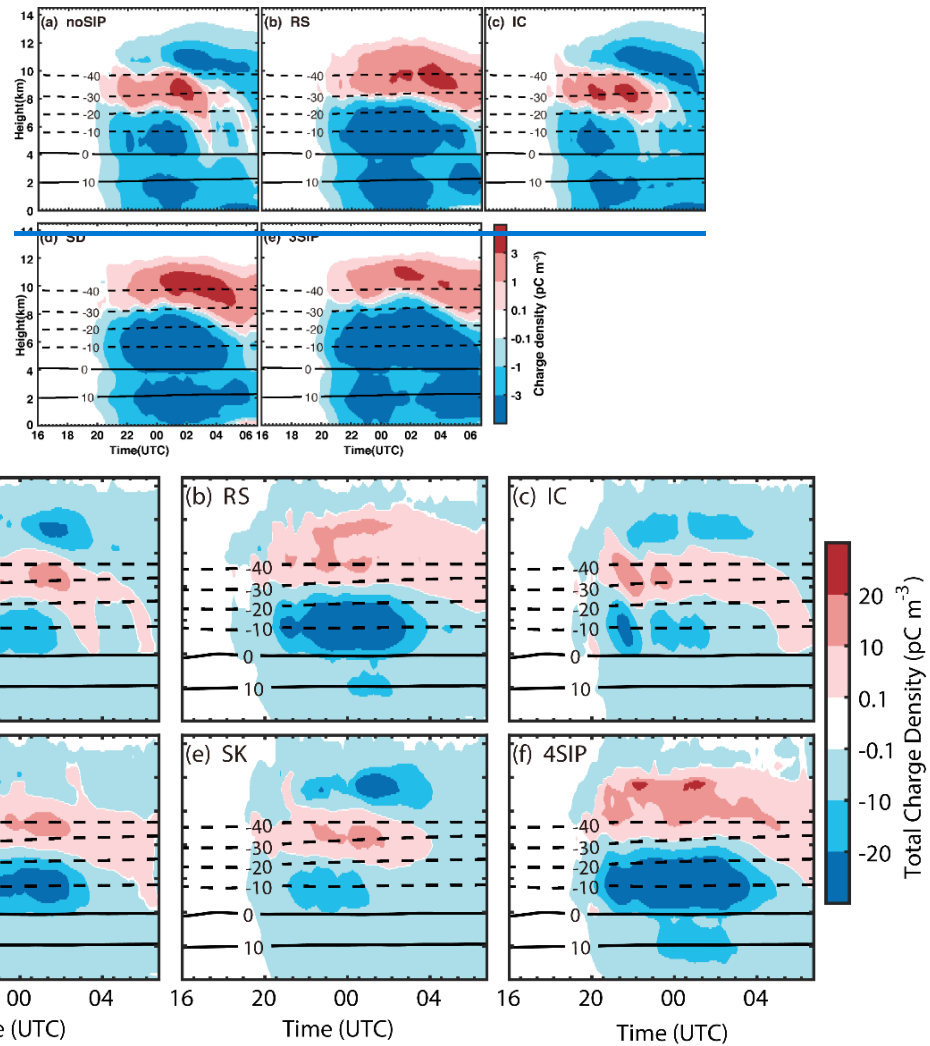
585 **Figure 11~~12~~18: Time-height diagrams of the total charge density (colored) and temperature (contours) from the ~~five~~ six numerical experiments. (a) experiment without SIP, (b) experiment with rime-splintering, (c) experiment with ice-ice collisional breakup, (d) experiment with shattering of freezing drops, (e) experiment with sublimational breakup, and (e~~f~~) experiment with ~~three~~ four SIP processes.**

590 The structure of the average charge density shown Fig. ~~11~~18 looks fairly simple, however, the actual charge structure along a given cross~~-~~section is complicated~~, and it may change rapidly with time~~. Figure ~~12~~19 shows the cross~~-~~section of the total charge density ~~along 118~~117°E, 30°N ~~– 121~~119°E, 30°N. In general, if no SIP is considered, there is a main upper negative and a main middle positive charge region, a weak negative charge region is observed sometimes at the bottom of the cloud. The IC and SK experiments show the similar structure to noSIP. But the charge structure could be different at different locations, suggesting complicated microphysics processes. Due to the presence of ~~some lower~~ small positive charge regions at

low-levels, the charge structure ~~of~~in RS and SD experiments vary significantly along the cross--section (Fig. 19-b and d). With all the SIP processes considered, the storm obtains ~~an opposite~~a different charge structure compared to that in noSIP experiment, as there is a main positive charge region at the top and a main ~~middle~~negative charge region below. ~~Weak~~Small positive charge region~~s are~~is present at some locations near -10~~0~~ °C~~, this is probably the reason for the negative inductive charging rate on graupel at -10 °C (Fig. 9j16l)~~, but it cannot be intuitively revealed after averaging (Fig. ~~11e~~18f). The substantial change in the charge structure induced by SIP suggesting the charge separation in this storm is very sensitive to the ice and graupel generation (i.e., increase in ice and graupel mixing ratio and number concentration).

Figure 19: Cross sections of the modelled total charge density from the six numerical experiments. (a) experiment without SIP, (b) experiment with rime-splintering, (c) experiment with ice-ice collisional breakup, (d) experiment with shattering of freezing drops, (e) experiment with sublimational breakup, and (f) experiment with four SIP processes.

~~Based on the equation~~According to Eq. B1 shown in Appendix B, we can see the charge transfer is determined by three terms: 1) charge transferred during each collision between graupel and ice (δq_{gi}); 2) collision kernel between graupel and ice; 3) concentration of graupel and ice. δq_{gi} is determined by RAR, which is a function of liquid water content (LWC) and terminal

velocity of graupel. With the addition of SIP, the LWC generally decreases (Fig. 8), and the diameters of ice particles decrease as well (Fig. 10), leading to a decrease in RAR (Fig. 2~~0~~~~1~~), especially in RS and SD experiments. The collision kernel between graupel and ice is determined by the terminal velocity and size of graupel and ice, which also decreases after SIP processes are implemented. The concentration of graupel (n_g) and ice (n_i) increases due to the ~~RS and SD~~rime-splintering and shattering

620 of freezing drops ~~processes~~, this explains the enhanced electrification by these two SIP processes. ~~Therefore, the higher graupel and ice concentration induced by RS and SD processes is the main reason resulting in the enhanced electric field, which leads to more flash rate after 00:00, Nov 28th.~~.
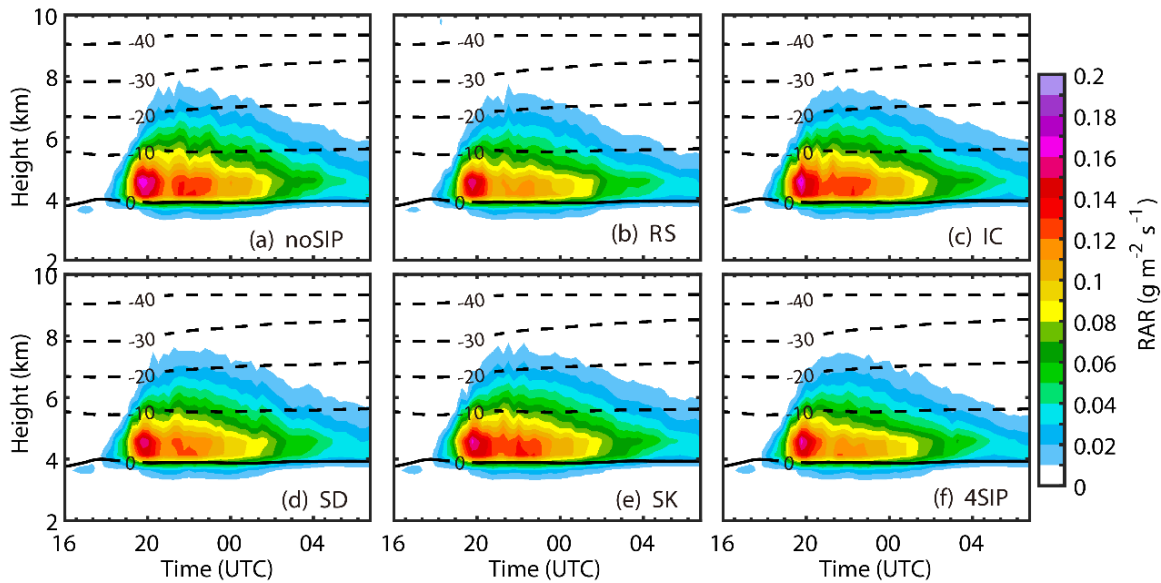
625 **Figure 2~~1~~0: Time-height diagrams of the RAR from the six numerical experiments. (a) experiment without SIP, (b) experiment with rime-splintering, (c) experiment with ice-ice collisional breakup, (d) experiment with shattering of freezing drops, (e) experiment with sublimational breakup, and (f) experiment with four SIP processes.**

630 Changes in the structure of total charge density result in changes in the electric field by the SIP processes. Figure ~~13~~ 2~~0~~1 shows the time-height diagram of the vertical electric field model~~l~~ed in different experiments, it is evident that the electric field is enhanced by the SIP, especially by the rime-splintering and shattering of freezing drops. The IC and SK experiments have the similar electric field to noSIP. The rime-splintering and shattering of freezing drops enhance the vertical electric field after 00:00, Nov. 28th (Fig. ~~13~~ 20b and d)~~, therefore, the lightning frequency after that time is as high as that before, this is different

635 from that in the noSIP and IC experiment, in which the lightning frequency rapidly decreased after 00~~04~~:00, Nov. 28th~~.~~ With all ~~the three SIP processes~~ implemented, the eclectic field is clearly enhanced, especially after 00:00, Nov. 28th (Fig. ~~13e~~20f), resulting in higher lightning frequency in the entire period.
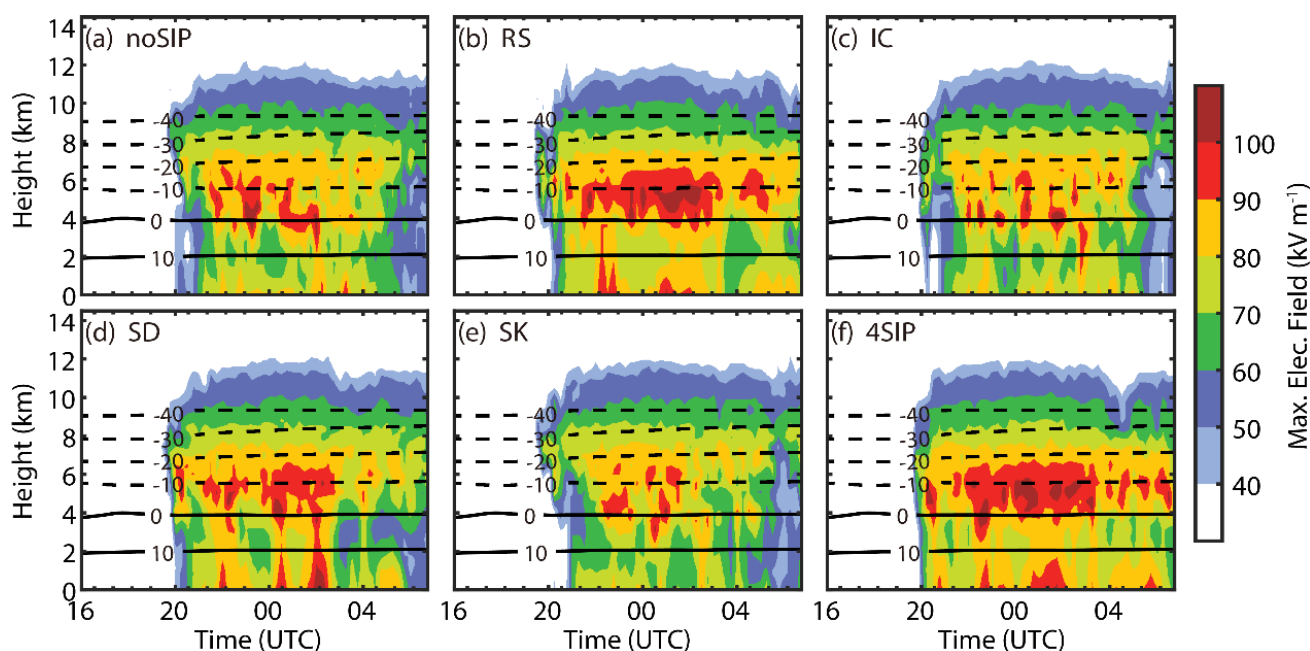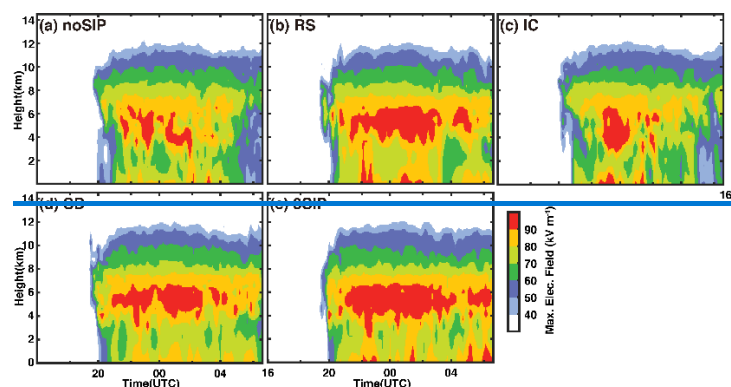
Figure ~~13~~14 2~~0~~1: Time-height diagrams of the maximum vertical electric field from the ~~five~~ six numerical experiments.
(a) experiment without SIP, (b) experiment with rime-splintering, (c) experiment with ice-ice collisional breakup, (d)
experiment with shattering of freezing drops, (e) experiment with sublimational breakup, and (~~e~~f) experiment with
~~three~~ four SIP processes.

~~5~~ 4 Discussion and Conclusions

In this study, the impacts of different SIP processes on the cloud electrification in a cold-season thunderstorm is investigated using WRF model simulations with SBM microphysics scheme. The storm occurred in late November in southeast China. ~~Three~~ Four SIP processes are considered in the model, including the rime-splintering, the ice-ice collisional breakup, ~~and~~

shattering of freezing drops, and sublimational breakup. In addition, a noninductive and an inductive charging parametrization,
as well as a bulk discharging model are coupled with the SBM microphysics. The impacts of different SIP processes on the
cloud microphysics and electrification are compared using ~~five~~ six sensitivity experiments, one control run without SIP, one
with all the ~~three~~ four SIP processes, and ~~three~~ four in each a single SIP is used. The results contribute to fill the dearth of
understanding the impact of different SIP processes on the cloud electrification in cold-season thunderstorms.

Comparison between model simulation and observation suggests the model well captures the scale and east propagation of the
storm. The SIP has minor impacts on the macro-properties of the storm, while the intensity can be affected. If no SIP is
considered, the model overestimates the composite radar reflectivity. ~~The ice-ice collisional breakup and sublimational breakup~~
~~haves minor impacts on the radar reflectivity, while if rime-splintering or shattering of freezing drops is used, the modelled~~
~~radar reflectivity is reduced.~~ With all the ~~three~~ four SIP processes implemented, the simulation result (composite radar
reflectivity and CFAD) is more consistent with the observation. This is mainly because the SIP processes suppress the sizes of
graupel and snow, though their concentration can be enhanced. The implementation of SIP also improves the simulation of
flash rate. Without any SIP, the ~~peak flash rate is obtained earlier than observed~~ lightning activity dissipated more rapidly. ~~The~~
~~ice-ice collisional break up and sublimational breakup enhances the flash rate but does not change the temporal variation peaks~~
~~at the same moment of observation. The rime-splintering and shattering of freezing drop can improve the temporal variability~~
~~of flash rate.~~ With all the ~~three~~ four SIP implemented, both the temporal variation and magnitude of the flash rate
are more consistent with the observation.

Different SIP processes have different impacts on the cloud microphysics electrification. The rime-splintering and shattering
of freezing drops are active throughout the cloud life cycle but are limited to relatively warm temperatures. The cloud glaciation
below 8 km is enhanced by these two processes, leading to lower LWC at higher levels. The low-level positive charging is
significantly enhanced by them due to the higher graupel and ice/snow concentrations. The ice-ice collisional breakup is more
active in regions with higher ice/snow mixing ratio, its average impact on cloud electrification is minor, while it could be
significant in some areas in the cloud. The sublimational breakup of snow is more active near cloud edges or in downdrafts,
and its average impact on cloud electrification is weak. Among the four SIP processes, rime-splintering has the greatest impact
on the cloud microphysics and its ice production rate is higher than the others, while the impact of sublimational breakup of
ice is the weakest, and its ice production rate is the lowest.

~~The enhanced graupel and ice mixing ratio and concentration would affect the charging rate by enhancing the collision between~~
~~graupel and ice, as well as the riming process.~~ In the case presented in this paper, the noninductive charging rate has a reversal

at -20 °C, with negative charging on graupel above this level, and positive charging below. Without SIP considered, the magnitude of the upper-level negative charging rate is slightly larger than the positive charging rate. With rime-splintering or shattering of freezing drops included, the positive charging rate is substantially enhanced. The inductive charging rate is a few times smaller the noninductive charging rate, and the SIP can change the upper-level inductive charging on graupel from negative to positive. The changes in the charging rate due to SIP result in substantial modification of the charge structure. The charge density carried by graupel and snow below -20 °C obtain an opposite sign after SIP is implemented in the model. The total charge density changes from an inverted tripole structure to a dipole structure (tripole structure at some locations) after four SIP processes are~~is~~ implemented in the model. These changes lead to an enhancement of vertical electric field, especially in the mature stage~~, which explains the improved temporal variation of flash rate in the model~~.

Due to the scarcity of winter thunderstorms, there have been few modelling studies of it. Takahashi et al. (2019) studied the winter clouds in Hokuriku and found that lightning was generated in clouds with the following conditions: cloud top temperature less than -14~~℃~~ °C, -10 ~~℃~~°C isotherm is higher than 1.2 km, space charge greater than 2-3 pC ~~/~~L^{-1}, ice crystal concentration greater than 500 m^{-3}, and graupel concentration greater than 20 m^{-3}. According to the analysis above, the thundercloud studied in this paper satisfies all these characteristics. Takahashi et. al. (2017) pointed out that winter thunderstorm clouds have lower LWC and low cloud tops than summer time convections. In our simulation, the modeled LWC is typically lower than 1 g m^{-3}, which is lower than that reported in summer ~~convections~~convective clouds (e.g., Yang et al., 2016; Phillips et al. 2022). The lower LWC in wintertime convection indicates weaker riming, thus a lower ~~riming accretion rat~~RAR~~e~~, which potentially leads to a higher possibility of inverted charge structure of thunderstorms (Wang et al. 2021). In many previous studies of summertime thunderstorms that occurred at a similar latitude (e.g., Caicedo et al., 2018; Shi et al., 2015), the main charging region is typically at 5-11 km a.m.s.l., and the freezing level is at about 5 km a.m.s.l, which are all about 1 km higher than the cold-season storm shown in this paper. ~~The ambient temperature near surface in this cold-season storm is approximately 10 °C lower than that in summer. Kitagawa and Michimoto (1994) found that wintertime thunderstorms generally have shorter periods of electrical activity and less frequent lightning than summer thunderstorms. In addition, they noted that the tropopause remains at 16 km in summer and drops to 10 km in winter, and the vertical extent of the atmospheric circulation is about half that of summer. This is the main factor that limits the convective activity of thunderstorm clouds in winter.~~

~~Observational studies suggest there are a variety of charge structures in different thunderstorms (Qie et al., 2019). Unfortunately, we do not have charge measurement in this case, so we are not able to evaluate the modelled charge structure. But the result in the simulation with three~~ four ~~SIP processes is consistent with many observational studies of cold-season thunderstorm, though occurred in different regions (e.g., Kitagawa and Michimoto, 1994; Takahashi et al., 1999, 2018, 2019; Yoshida et al., 2018; Zheng et al., 2018). Takahashi et al. (1999, 2018) investigated the evolution of charge structure in~~

Hokuriku winter thunderstorms, and they suggested that the charge separation of graupel is observed at -10 °C. Graupel embryos forms at temperatures lower than -10 °C, and continued growing through riming. The graupel gets negative charging when it collides with ice crystals at temperatures colder than -10 °C. While it gets positive charging if falling it falls to levels warmer than -10 °C. This result is consistent with our finding, except that the sign of charging on graupel reversed at -20 °C in the present study.

Some studies suggested the charge separation in thunderstorm is sensitive to the parametrization of electrification (Altaratz et al., 2005; Fierro et al., 2013; Xu et al., 2019). Here, we highlight that the cold-season cloud electrification is also sensitive to the SIP. However, the results shown here only reveal the relative importance of three four SIP mechanisms on in a single case. While in other cases, the SIP processes may have different impacts on the charge structure. For example, Phillips and Patade (2022) suggested in summertime thunderstorms with high cloud base, the ice-ice collisional breakup has stronger impacts than the other SIP mechanisms, which is different from the result shown in this paper. Huang et al. (2022) analyzed the relative contribution of 3 SIP processes to ice generation using model simulations, they compared the modeled microphysics to airborne observation, and the results show shattering of freezing droplets dominates ice particle production at temperatures between -15 °C and 0 °C during the developing stage of convection, and ice-ice collisional breakup dominates at temperatures during the later stage of convection. Studies that investigate the impacts of different SIPs on cloud electrification are still limited. It will be interesting to see how changes in different environmental conditions (such as wind shear, cloud base height, and aerosol and INP concentrations) in different cases would influence the role of different SIPs. Based on this study, it is suggested that sufficient graupel is important for SIP processes to enhance cloud electrification.

Future work includes more studies of different cases and improvement of the parameterizations. Currently, there are still some assumptions used in the parameterizations, for instance, the rimed fraction of ice crystals, which influences the efficiency of the ice-ice collision (Karalis et al., 2022; Sotiropoulou et al., 2021), is assumed constant in this study. A sensitivity test shows using a larger rimed fraction can result in a stronger impact of ice-ice collisional breakup on cloud microphysics and electrification (not shown). Therefore, future laboratory and field measurements would be helpful to determine these parameters. Some other ice processes that are not considered in the model may also influence cloud electrification, such as ice fragmentation due to thermal shock (Korolev et al., 2020) and pre-activation of ice nucleating particles (Jing et al., 2022). It is worth investigating the impacts of these mechanisms using model simulations once there are sufficient measurements to support the development of parameterizations in the future.

This indicates factors such as the dynamics and thermodynamics of storms may control the role of SIP in thunderstorms. In addition, only three four SIP mechanisms are implemented in the model in this study, because these SIP processes are important in convective clouds and there are observational datasets available for developing the parameterizations. Some other SIP mechanisms may also contribute to the ice generation, such as the breakup of snow during sublimation, INPs actived by

Appendix A

Based on laboratory experiment, Hallett and Mossop (1974) showed one ice splinter can be generated during riming process for every 200 droplets collected by a graupel. The ice splinter production rate of rime-splintering N_{RS} is:

$$N_{RS} = 3.5 \cdot 10^5 \cdot \left(\frac{\partial m_g}{\partial t}\right) \cdot R_{rim}(T) \tag{A1}$$

$$R_{rim}(T) = \begin{cases} 0, & T \geq 270.16K \\ (T - 268.16)/2, & 268.16K \leq T < 270.17K \\ (T - 268.16)/3, & 265.16K \leq T < 268.16K \\ 0, & T < 265.16K \end{cases} \tag{A2}$$

where, $\frac{\partial m_g}{\partial t}$ indicates the riming rate, T is the temperature.

The parametrization of ice–ice collisional breakup is developed by Phillips et al. (2017). The number of ice fragments produced during ice–ice collision is:

$$N_{IC} = \alpha A(M) \left\{ 1 - \exp\left[- \left(\frac{C(M)K_0}{\alpha A(M)} \right)^\gamma \right] \right\} \tag{A3}$$

where A(M) is the number density of breakable asperities on the ice particle and related to the rimed fraction and the size of smaller ice particle, C(M) is asperity–fragility coefficient that is set as 3.86×10^4 according to the cloud chamber experiment of natural ice particles (Gautam, 2022), K_0 is the initial value of collision kinetic energy, γ and α are the shape parameter and the equivalent spherical surface area of smaller particles, respectively. $\gamma = 0.5 - 0.25\Psi$, where Ψ denotes the rimed fraction, which is assumed 0.2 in this study. The tiny fragments are treated as the ice particles belonging to the first bin of the Fast-SBM model. In WRF SBM, the collision efficiency between ice crystals is obtained based on the Bohm's theory (Bohm, 1992a, 1992b) and the superposition method in Khain et al. (2001). The coalescence efficiency is parameterized based on Khain and Sednev (1996), which is a function of vapor pressure and temperature.

780

The parameterization of shattering of freezing drops ~~is~~ was developed by Phillips et al. (2018) based on laboratory experiments. If contacting with a smaller ice particle, a supercooled drop may breakup and produce both big and tiny ice fragments, thus, the number of the ice fragments can be expressed using:

$$N_{SD\_1} = N_T + N_B \tag{A4}$$

785

$$N_{SD\_1T} = F(D)\Omega(T)\left[\frac{\xi_T \eta_T^2}{(T-T_{T,0})^2 + \eta_t^2} + \beta T\right] \tag{A5}$$

$$N_B = \min\left\{F(D)\Omega(T)\left[\frac{\xi_B \eta_B^2}{(T-T_{B,0})^2 + \eta_B^2}\right], N_T\right\} \tag{A6}$$

where, N_T and N_B are the number of tiny and big ice fragments generated by a shattered drop. $F(D)$ and $\Omega(T)$ are the interpolating functions for the onset of drop shattering. $\xi_T, \xi_B, \eta_T, \eta_B, T_{T,0}, T_{B,0}, \beta$, are parameters determined based on datasets from previous laboratory experiments, which can be found in Phillips et al. (2018). The tiny fragments are treated as

790   the ice particle belonging to the first bin of Fast-SBM model, which have a diameter of 4 micrometers (Khain et al., 2004). The mass of big ice fragments is $m_B = 0.4 m_{drop}$.

In addition, a drop may also break if contacting with a more massive ice particle. The number of ice fragments produced in this process is:

795

$$N_{SD\_2} = 3\Phi \times [1 - f(T)] \times \max\left\{\left(\frac{k_0}{S_e} - DE_{crit}\right), 0\right\} \tag{A7}$$

$$f(T) = \frac{-C_w T}{L_f} \tag{A8}$$

$$S_e = \gamma_{liq}\pi D^2 \tag{A9}$$

where, γ_{liq} is the surface tension of liquid drop, k_0 is the initial kinetic energy of the two colliding particles, $f(T)$ is the frozen fraction. C_w and L_f are the specific heat capacity of water and the specific latent heat of freezing, respectively. $DE_{crit} = 0.2$,

800   and Φ is 0.3 according to James et al. (2021). All ice fragments are assumed to be tiny in this mode. The tiny ice fragments are added to the first bin of ice size distribution, ~~and the mass of big ice fragments is $m_B = 0.4 m_{drop}$~~.

The parameterization of sublimational breakup is proposed by Deshmukh et al. (2022). The number of ice splinters produced during sublimation is depended on the relative humidity on the ice and the preliminary size of the mother ice particles. The

805   formulation is used for dendritic crystals and heavily rimed particles (e.g., graupel). The rate of ice splinters produced by dendritic crystals is:

$$\frac{dN}{dt} \approx \beta d^\gamma d(100 - RH_i)f_v\Xi\nu \tag{A10}$$

$$\nu(RH_i, d) = \Delta_0^1[RH_i, RH_{i0}(d), RH_{i0}(d) + \Delta RH_i] \tag{A11}$$

$$RH_{i0} = 72\lambda + 94(1 - \lambda) \tag{A12}$$

810 where, d refers to the diameter of parent ice particels, RH_i represents the relative humidity over ice, f_v denotes ventilation coefficient for vapor diffusion, Ξ is emission factor, v is onset transition factor for dendrites, λ is size dependent fraction. β and λ are empirical parameters. $\Delta RH_i = 6\%$.

$$\frac{dN}{dt} \approx \frac{\rho_{D0}}{\rho_r} \beta d^\gamma d(100 - RH_i) f_v \Xi v^* \tag{A13}$$

$$v^*(RH_i, d) = \Delta_0^1[RH_i, RH_{i0}(d), RH_{i0}(d) + (1 + 2\lambda)\Delta RH_i] \tag{A14}$$

815 ρ_r denotes the density of a rimed particle. ρ_{D0} is observed density by Dong et al. (1994). $\rho_{D0} = 300 \ kg \ m^{-3}$. v^* is onset transition factor for graupel, and mass of ice fragments is $m_f = \chi m_{ice}$.

Appendix B

The non-inductive charging produced during the collision between graupel and ice crystal is expressed as:

820
$$\frac{\partial \rho_{gi}}{\partial t} = \iint_0^\infty \frac{\pi}{4} \beta \delta q_{gi} (1 - E_{gi}) |V_g - V_i| (D_g + D_i)^2 n_g n_i dD_g dD_i \tag{B1}$$

$$\beta = \begin{cases} 1, & T > -30 \ ℃ \\ 1 - \left[\frac{T+30}{13}\right]^2, & -43 \ ℃ < T < -30 \ ℃ \\ 0, & T < -43 \ ℃ \end{cases} \tag{B2}$$

where, T is temperature. E_{gi} is collection efficiency between graupel and ice. V, D and n are the terminal velocity, diameter, and number concentration, with subscripts g and i indicate graupel and ice crystals. The charge transferred per rebounding collision (δq_{xy}) is a function of rime accretion rate (RAR) ~~(riming accretion rate)~~ and critical RAR (RAR$_c$) (Saunders and

825 Peck 1998):

$$\delta q_{xy} = B d^a V^b \delta q_\pm \tag{B3}$$

where, B, a and b are parameters determined based on laboratory studies. For positive charging of graupel (RAR > RAR$_c$),

$$\delta q_+ = 6.74(RAR - RAR_c) \tag{B4}$$

and for negative charging ($0.1 gm^{-2}s^{-1} < RAR < RAR_c$),

830
$$\delta q_- = 3.9(RAR_c - 0.1)\left\{4\left[\frac{RAR - (RAR_c + 0.1)/2}{RAR_c - 0.1}\right]^2 - 1\right\} \tag{B5}$$

$$RAR_c = \begin{cases} s(T), & T > -23.7℃ \\ k(T), & -23.7℃ > T > -40℃ \\ 0, & T \le -40℃ \end{cases} \tag{B6}$$

$$s(T) = 1.0 + 7.9262 \cdot 10^{-2}T + 4.4847 \cdot 10^{-2}T^2 + 7.4754 \cdot 10^{-3}T^3 + 5.4686 \cdot 10^{-4}T^4 + 1.6737 \cdot 10^{-5}T^5 + 1.7613 \cdot 10^{-7}T^6 \tag{B7}$$

$$k(T) = 3.4[1.0 - \left(\frac{|T+23.7|}{-23.7+40.0}\right)^3] \tag{B8}$$

835

According to Mansell et al. (2005), the inductive charging rate is parametrized as:

$$\frac{\partial \rho_g}{\partial_t} = \left(\frac{\pi^3}{8}\right)\left(\frac{6.0\bar{V}_g}{\Gamma(4.5)}\right)E_{gc}E_r n_c n_{0g} D_c^2 \times [\pi\Gamma(3.5)\epsilon\langle cos\theta\rangle E_z \mathcal{D}_g^2 - \Gamma(1.5)\frac{\rho_g}{3n_g}] \tag{B9}$$

where, E_{gc} is the collision efficiency between graupel and droplet. E_r is the rebound probability. n_c is the number concentration of cloud droplet. n_{0g} is the intercept of graupel size distribution. θ is the rebounding collision angle. ϵ is the

840   permittivity of air. E_z is the vertical electric field, and ρ_g is the charge density carried by graupel.

The discharge model used in this paper is a bulk discharge scheme suggested by Fierro et al. (2013), in which flash occurs once the electric field exceeds a threshold. The electric field (E) can be computed by solving the Poisson equation:

$$\nabla^2 \emptyset = -\frac{\rho_{tot}}{\epsilon} \tag{B10}$$

845

$$E = -\nabla\emptyset \tag{B11}$$

where, ρ_{tot} is the net charge density.

Data availability

The WRF model is available on https://www.mmm.ucar.edu/models/wrf. The reanalysis data used to drive WRF model is available on https://www.ecmwf.int/en/forecasts/dataset/ecmwf-reanalysis-

850   v5https://rda.ucar.edu/datasets/ds083.2/dataaccess/. The observed radar reflectivity images, sounding data and lightning data are available on https://doi.org/ 10.5281/zenodo.8371845.

Author contributions

SH and JY implemented the parametrizations of SIP and electrification in WRF, and designed the numerical experiments. SH, JY, and YL performed the analysis and prepared the manuscript. TY, QZ and YD contribute to the model evaluation. TY and

855   QZ and XJ provided input on the method and analysis. All authors provided significant feedback on the manuscript.

Competing interests

The contact author has declared that none of the authors has any competing interests.

Acknowledgements

This work was supported the National Key R&D Program of China (Grant No. 2023YFC3000067), the National Natural Science Foundation of China (41905124), the Natural Science Foundation of Jiangsu Province, China (BK20190778), and the CMA Key Innovation Team Support Project (CMA2022ZD10). We appreciate the editor and reviewers for their insightful comments and suggestions.

References

Altaratz, O., Reisin, T. and Levin, Z.: Simulation of the electrification of winter thunderclouds using the three-dimensional regional atmospheric modeling system (RAMS) model: Single cloud simulations. Journal of Geophysical Research: Atmospheres, 110, D20, doi: 10.1029/2004JD005616, 2005.

Baker, M. B., Christian, H. J., and Latham, J.: A computational study of the relationships linking lightning frequency and other thundercloud parameters. Quarterly Journal of the Royal Meteorological Society, 121, 1525–1548, doi: 10.1002/qj.49712152703, 1995.

Brook, M.: Breakdown electric fields in winter storms. Journal of Atmospheric Electricity, 12, 47-52, doi: 10.1541/jae.12.47, 1992.

Brooks, M. I., Saunders, C. P. R., Mitzeva, R. P., and Peck, S. L.: The effect on thunderstorm charging of the rate of rime accretion by graupel. Atmos. Res., 43, 277–295, doi: 10.1175/MWR-D-12-00278.1, 1997.

Caicedo, J. A., Uman, M. A., and Pilkey, J. T.: Lightning evolution in two North Central Florida summer multicell storms and three winter/spring frontal storms. Journal of Geophysical Research: Atmospheres, 123, 1155–1178, doi: https://doi.org/10.1002/2017JD026536, 2018.

Deshmukh, A., Phillips, V. T. J., Bansemer, A., Patade, S., and Waman, D.: New Empirical Formulation for the Sublimational Breakup of Graupel and Dendritic Snow. Journal of the Atmospheric Sciences, 79(1), 317–336, doi: https://doi.org/10.1175/JAS-D-20-0275.1, 2022.

Dong, Y., Oraltay, R. G., and Hallett, J.: Ice particle generation during evaporation. Atmospheric Research, 32(1-4), 45–53, doi:10.1016/0169-8095(94)90050-7, 1994.

Emersic, C., and Saunders, C. P. R.: Further laboratory investigations into the relative diffusional growth rate theory of thunderstorm electrification. Atmos. Res., 98, 327–340, doi: 10.1016/j.atmosres.2010.07.011, 2010.

Fan, J., L. R. Leung, Z. Li, H. Morrison, H. Chen, Y. Zhou, Y. Qian, and Y. Wang: Aerosol impacts on clouds and precipitation in eastern China: Results from bin and bulk microphysics. J. Geophys. Res., 117, D00K36, doi:10.1029/2011JD016537, 2012.

Fierro, A. O., Mansell, E. R., MacGorman, D. R., and Ziegler, C. L.: The Implementation of an Explicit Charging and Discharge Lightning Scheme within the WRF-ARW Model: Benchmark Simulations of a Continental Squall Line, a Tropical Cyclone, and a Winter Storm. Monthly Weather Review, 141, 2390–2415, doi: 10.1175/MWR-D-12-00278.1, 2013.

890 Gautam, M.: Fragmentation in graupel snow collisions. Master of Science dissertation, Dept of Physical Geography and Ecosystem Science, Lund University, Lund, Sweden-, doi: http://lup.lub.lu.se/student-papers/record/9087233, 2022.

Guo, F., Li, Y., Huang, Z., Wang, M., Zeng, F., Lian, C. and Mu, Y.:Numerical simulation of 23 June 2016 Yancheng City EF4 tornadic supercell and analysis of lightning activity. Science China Earth Sciences, 60, 2204-2213, doi: 10.1007/s11430-017-9109-8, 2017.

Hallett, J., and Mossop, S. C.: Production of secondary ice particles during the riming process. Nature, 249, 26–28, doi: doi:
895 10.1038/249026a0, 1974.

Heymsfield, A. and Willis, P.: Cloud conditions favoring secondary ice particle production in tropical maritime convection. J. Atmos. Sci., 71, 4500–4526, doi: 10.1175/JAS-D-14-0093.1, 2014.

Hong, S.-Y., Noh, Y., and Dudhia, J.: A New Vertical Diffusion Package with an Explicit Treatment of Entrainment Processes. Monthly Weather Review, 134, 2318–2341, doi: 10.1175/MWR3199.1, 2006.

900 Huang, Y., Wu, W., McFarquhar, G. M., Xue, M., Morrison, H., Milbrandt, J., Korolev, A. V., Hu, Y., Qu, Z., Wolde, M., Nguyen, C., Schwarzenboeck, A., and Heckman, I.: Microphysical processes producing high ice water contents (HIWCs) in tropical convective clouds during the HAIC-HIWC field campaign: Dominant role of secondary ice production. Atmospheric Chemistry and Physics, 22(4), 2365–2384, https://doi.org/10.5194/acp-22-2365-2022, 2022.

James, R. L., Phillips, V. T. and Connolly, P. J.: Secondary ice production during the break-up of freezing water drops on
905 impact with ice particles. Atmospheric Chemistry and Physics, 21, 18519-18530, doi: 10.5194/acp-21-18519-2021, 2021.

Jiménez, P. A., Dudhia, J., González-Rouco, J. F., Navarro, J., Montávez, J. P., and García-Bustamante, E.: A Revised Scheme for the WRF Surface Layer Formulation. Monthly Weather Review, 140, 898–918, doi: 10.1175/MWR-D-11-00056.1, 2012.

Jing, X., Yang, J., Li, T., Hu, J., He, C., Yin, Y., DeMott, P. J., Wang, Z., Jiang, H., Chen, K.: Pre-activation of ice nucleating particles in deposition nucleation mode: Evidence from measurement using a static vacuum water vapor diffusion chamber in
910 Xinjiang, China. Geophysical Research Letters, 49, e2022GL099468, doi: 10.1029/2022GL099468, 2022.

Kain, J. S.: The Kain–Fritsch Convective Parameterization: An Update. Journal of Applied Meteorology, 43, 170–181, doi: 10.1175/1520-0450(2004)043<0170:TKCPAU>2.0.CO;2, 2004.

Karalis, M., Sotiropoulou, G., Abel, S. J., Bossioli, E., Georgakaki, P., Methymaki, G., Nenes, A. and Tombrou, M.: Effects of secondary ice processes on a stratocumulus to cumulus transition during a cold-air outbreak, Atmos. Res., 277,
915 doi:10.1016/j.atmosres.2022.106302, 2022.

Khain, A., Pokrovsky, A., Pinsky, M., Seifert, A., and Phillips, V.: Simulation of Effects of Atmospheric Aerosols on Deep Turbulent Convective Clouds Using a Spectral Microphysics Mixed-Phase Cumulus Cloud Model. Part I: Model Description and Possible Applications. Journal of the Atmospheric Sciences, 61, 2963–2982, doi: 10.1175/JAS-3350.1, 2004.

920 Khain, A. P., et al. : Representation of microphysical processes in cloud- resolving models: Spectral (bin) microphysics versus bulk parameterization. Rev. Geophys., 53, 247–322, doi:10.1002/2014RG000468, 2015.

King, W. D., and Fletcher, N. H.: Pressures and stresses in freezing water drops. Journal of Physics D: Applied Physics, 6, 2157–2173, doi: 10.1088/0022-3727/6/18/302, 1973.

Kitagawa, N., and Michimoto, K.: Meteorological and electrical aspects of winter thunderclouds. Journal of Geophysical Research, 99(D5), 10713, https://doi.org/10.1029/94JD00288, 1994.

925 Korolev, A., and Leisner, T.: Review of experimental studies of secondary ice production. Atmospheric Chemistry and Physics, 20, 11767–11797, doi: 10.5194/acp-20-11767-2020, 2020.

Latham, J., Blyth, A. M., Christian, H. J., Deierling, W., and Gadian, A. M.: Determination of precipitation rates and yields from lightning measurements. Journal of Hydrology, 288(1–2), 13–19, doi: 10.1016/j.jhydrol.2003.11.009, 2004.

Lauber, A., Kiselev, A., Pander, T., Handmann, P., and Leisner, T.: Secondary Ice Formation during Freezing of Levitated
930 Droplets. Journal of the Atmospheric Sciences, 75, 2815–2826, doi: 10.1175/JAS-D-18-0052.1, 2018

Li, J.; Dai, B.; Zhou, J.; Zhang, J.; Zhang, Q.; Yang, J.; Wang, Y.; Gu, J.; Hou, W.; Zou, B, and Li, J.: Preliminary Application of Long-Range Lightning Location Network with Equivalent Propagation Velocity in China. Remote Sens. 14, 560, doi: 10.3390/rs14030560, 2022.

Lyu, W., Zheng, D., Zhang, Y., Yao, W., Jiang, R., Yuan, S., Liu, D., Lyu, F., Zhu, B., Lu, G. and Zhang, Q.: A Review of
935 Atmospheric Electricity Research in China from 2019 to 2022. Advances in Atmospheric Sciences, 40, 1457-1484, doi: 10.1007/s00376-023-2280-x, 2023.

Mansell, E. R., MacGorman, D. R., Ziegler, C. L., and Straka, J. M., Charge structure and lightning sensitivity in a simulated multicell thunderstorm. Journal of Geophysical Research, 110, D12101, doi: 10.1029/2004JD005287, 2005.

Mansell, E. R., Ziegler, C. L., and Bruning, E. C.: Simulated electrification of a small thunderstorm with two-moment bulk
940 microphysics. J. Atmos. Sci., 67, 171–194, doi: 10.1175/2009JAS2965.1, 2010.~~Mansell, E. R.: On Sedimentation and Advection in Multimoment Bulk Microphysics. Journal of the Atmospheric Sciences, 67(9), 3084-3094, doi: 10.1175/2010JAS3341.1, 2010.~~

Michimoto, K.: A study of radar echoes and their relation to lightning discharge of thunderclouds in the Hokuriku district Part I: Observation and analysis of thunderclouds in summer and winter. Journal of the Meteorological Society of Japan. Ser. II,
945 69, 327-336, doi: 10.2151/jmsj1965.69.3_327, 1991.

Mlawer, E. J., Taubman, S. J., Brown, P. D., Iacono, M. J., and Clough, S. A.: Radiative transfer for inhomogeneous atmospheres: RRTM, a validated correlated-k model for the longwave. Journal of Geophysical Research: Atmospheres, 102(D14), 16663–16682, doi: 10.1029/97JD00237, 1997.

Moore, C. B.: Rebound limits on charge separation by falling precipitation. Journal of Geophysical Research, 80, 2658–2662,
950 doi: 10.1029/JC080i018p02658, 1975.

Phillips, V. T. J., Yano, Jun-Ichi, Khain, A.: Ice Multiplication by Breakup in Ice-Ice Collisions. Part I: Theoretical Formulation. J. Atmos. Sci., doi: 10.1175/JAS-D-16-0224.1, 2017.

Phillips, V. T. J., Patade, S., Gutierrez, J., and Bansemer, A.: Secondary Ice Production by Fragmentation of Freezing Drops: Formulation and Theory. J. Atmos. Sci., 75, 3031–3070, doi: 10.1175/JAS-D-17-0190.1, 2018.

955 Phillips, V. T., Formenton, M., Kanawade, V. P., Karlsson, L. R., Patade, S., Sun, J., Barthe, C., Pinty, J. P., Detwiler, A. G., Lyu, W. and Tessendorf, S. A.: Multiple environmental influences on the lightning of cold-based continental cumulonimbus clouds. Part I: Description and validation of model. J. Atmos. Sci., 77, 3999-4024, doi: 10.1175/JAS-D-19-0200.1, 2020.

Phillips, V.T. and Patade, S.: Multiple Environmental Influences on the Lightning of Cold-Based Continental Convection. Part II: Sensitivity Tests for Its Charge Structure and Land–Ocean Contrast. J. Atmos. Sci., 79, 263–300, dio: 10.1175/JAS-D-20-
960 0234.1, 2022.

Qie, X. S., and Zhang, Y. J.: A review of atmospheric electricity research in China from 2011 to 2018. Adv. Atmos. Sci., 36, 994−1014, doi: 10.1007/s00376-019-8195-x, 2019.

Qie, X. S., and Coauthors: A review of atmospheric electricity research in China. Adv. Atmos. Sci., 32, 169−191, doi: 10.1007/s00376-014-0003-z, 2015.

965 ~~Qu, Y., Khain, A., Phillips, V., Ilotoviz, E., Shpund, J., Patade, S., & Chen, B. : The role of ice splintering on microphysics of deep convective clouds forming under different aerosol conditions: Simulations using the model with spectral bin microphysics. Journal of Geophysical Research: Atmospheres, 125, e2019JD031312, https://doi.org/10.1029/2019JD031312, 2020.~~

Saunders, C. P. R., and Peck, S. L.: Laboratory studies of the influence of the rime accretion rate on charge transfer during crystal/graupel collisions. Journal of Geophysical Research: Atmospheres, 103, 13949–13956, doi: 10.1029/97JD02644, 1998.

970 Saunders, C. P. R., Peck, S. L., Aguirre Varela, G. G., Avila, E. E., and Castellano, N. E.: A laboratory study of the influence of water vapour on the charge transfer process during collisions between ice crystals and graupel. Atmos. Res., 58, 187–203, doi: 10.1016/S0169-8095(01)00090-4, 2001.

Shi, Z., Tan, Y. B., Tang, H. Q., Sun, J., Yang, Y., Peng, L., and Guo, X. F.: Aerosol effect on the land-ocean contrast in thunderstorm electrification and lightning frequency. Atmospheric Research, 164–165, 131–141, doi:
975 10.1016/j.atmosres.2015.05.006., 2015.

Sotiropoulou, G., Vignon, E., Young, G., Morrison, H., O'Shea, S. J., Lachlan-Cope, T., Berne, A. and Nenes, A.: Secondary ice production in summer clouds over the Antarctic coast: An underappreciated process in atmospheric models, Atmos. Chem. Phys., 21, 755–771, doi:10.5194/acp-21-755-2021, 2021.

Sotiropoulou, G., Vignon, E., Young, G., Morrison, H., O'Shea, S. J., Lachlan-Cope, T., Berne, A. and Nenes, A.: Secondary
980 ice production in summer clouds over the Antarctic coast: An underappreciated process in atmospheric models, Atmos. Chem. Phys., 21, 755–771, doi:10.5194/acp-21-755-2021, 2021.

Takahashi, T.: A numerical simulation of winter cumulus electrification. Part I: Shallow cloud. Journal of Atmospheric Sciences, 40, pp.1257-1280, doi: 10.1175/1520-0469(1983)040<1257:ANSOWC>2.0.CO;2, 1983.

Takahashi, Nagao, Y., and Kushiyama, Y.: Possible High Ice Particle Production during Graupel–Graupel Collisions. J. Atmos.
985 Sci., 52(24), 4523–4527, doi: 10.1175/1520-0469(1995)052<4523:PHIPPD>2.0.CO;2, 1995.

Takahashi, T., Tajiri, T., and Sonoi, Y.: Charges on graupel and snow crystals and the electrical structure of winter thunderstorms. J. Atmos. Sci., 56, 1561–1578, doi: 10.1175/1520-0469(1999)056<1561:COGASC>2.0.CO;2, 1999.

Takahashi, T. and Miyawaki, K.: Reexamination of riming electrification in a wind tunnel. J. Atmos. Sci., 59, 1018–1025, doi: 10.1175/1520-0469(2002)059<1018:ROREIA>2.0.CO;2, 2002.

990 Takahashi, T., Sugimoto, S., Kawano, T., and Suzuki, K.: Riming Electrification in Hokuriku Winter Clouds and Comparison with Laboratory Observations. Journal of the Atmospheric Sciences, 74(2), 431–447, https://doi.org/10.1175/JAS-D-16-0154.1, 2017.

Takahashi, T., Sugimoto, S., and Kawano, T.: Microphysical structure and lightning initiation in Hokuriku Winter Clouds. XVI International Conference on Atmospheric Electricity, O-04-01, 17–22 June 2018, Nara city, Nara, Japan.

995 Takahashi, T., Sugimoto, S., Kawano, T., and Suzuki, K.: Microphysical structure and lightning initiation in Hokuriku winter clouds. Journal of Geophysical Research: Atmospheres, 124, 13,156–13,181, doi: 10.1029/2018JD030227, 2019.

Tewari, M., Chen, F., Wang, W., Dudhia, J., LeMone, M. A., Mitchell, K., Ek, M., Gayno, G., Wegiel, J., and Cuenca, R. H: Implementation and verification of the unified NOAH land surface model in the WRF model, 20th Conference on Weather Analysis and Forecasting/16th Conference on Numerical Weather Prediction. American Meteorological Society: Seattle, WA, 1000 US, 11–15, 2004.

Waman, D., Patade, S., Jadav, A., Deshmukh, A., Gupta, A. K., Phillips, V. T. J., Bansemer, A. and Demott, P. J.: Dependencies of Four Mechanisms of Secondary Ice Production on Cloud-Top Temperature in a Continental Convective Storm, J. Atmos. Sci., 79(12), 3375–3404, doi:10.1175/JAS-D-21-0278.1, 2022.

Wang, D., Zheng, D., Wu, T. and Takagi, N.: Winter positive cloud-to-ground lightning flashes observed by LMA in Japan. 1005 IEEJ Transactions on Electrical and Electronic Engineering, 16, 402-411, doi:10.1002/tee.23310, 2021

Xu, L. T., Zhang, Y. J., Wang, F., and Cao, X.: Simulation of inverted charge structure formation in convective regions of mesoscale convective system. J. Meteor. Soc. Japan, 97, 1119−1135, doi: 10.2151/jmsj.2019-062, 2019.

Yang, J., Wang, Z., Heymsfield, A., and Luo, T., Liquid-ice mass partition in tropical maritime convective clouds. J. Atmos. Sci., 73, 4959-4978, doi: 10.1175/JAS-D-15-0145.1, 2016.

1010 Yang, J., Wang, Z., Heymsfield, A. J., DeMott, P. J., Twohy, C. H., Suski, K. J., and Toohey, D. W.: High Ice Concentration Observed in Tropical Maritime Stratiform Mixed-Phase Clouds with Top Temperatures Warmer than -8 °C. Atmos. Res., 233, 104719, doi: 10.1016/j.atmosres.2019.104719, 2020.

Yano, J.-I., and Phillips, V. T. J.: Ice–Ice Collisions: An Ice Multiplication Process in Atmospheric Clouds. Journal of the Atmospheric Sciences, 68, 322–333, doi: 10.1175/2010JAS3607.1, 2011.

1015 Zhang, Y. J., and Coauthors: A review of advances in lightning observations during the past decade in Guangdong, China. J. Meteor. Res., 30, 800−819, doi: 10. 1007/s13351-016-6928-7, 2016.

Zheng, D., Wang, D., Zhang, Y., Wu, T., and Takagi, N.: Charge regions indicated by LMA lightning flashes in Hokuriku's winter thunderstorms. Journal of Geophysical Research: Atmospheres, 124, doi: 10.1029/2018JD030060, 2019.